AGU PUBLICATIONS

JGR

Journal of Geophysical Research: Solid Earth

RESEARCH ARTICLE
10.1002/2016JB013470

Key Points:
- A microphysical model explains rate and state friction
- Friction controlled by competition between granular flow and pressure solution

Supporting Information:
- Supporting Information S1

Correspondence to:
J. Chen,
jychen@ies.ac.cn

Citation:
Chen, J., and C. J. Spiers (2016), Rate and state frictional and healing behavior of carbonate fault gouge explained using microphysical model, *J. Geophys. Res. Solid Earth*, *121*, 8642–8665, doi:10.1002/2016JB013470.

Received 25 AUG 2016
Accepted 11 NOV 2016
Accepted article online 15 NOV 2016
Published online 3 DEC 2016

Rate and state frictional and healing behavior of carbonate fault gouge explained using microphysical model

Jianye Chen[1,2] and Christopher J. Spiers[2]

[1]State Key Laboratory of Earthquake Dynamics, Institute of Geology, China Earthquake Administration, Beijing, China, [2]HPT Laboratory, Department of Earth Sciences, Utrecht University, Utrecht, Netherlands

Abstract Classical rate-and-state friction (RSF) laws are widely applied in modeling earthquake dynamics but generally using empirically determined parameters with little or no knowledge of, or quantitative account for, the controlling physical mechanisms. Here a mechanism-based microphysical model is developed for describing the frictional behavior of carbonate fault gouge, assuming that the frictional behavior seen in lab experiments is controlled by competing processes of rate-strengthening intergranular sliding versus contact creep by pressure solution. By solving the controlling equations, derived from kinematic and energy/entropy balance considerations, and employing a microphysical model for rate-strengthening grain boundary friction plus standard creep equations for pressure solution, we simulate typical lab-frictional tests, namely, "velocity stepping" and "slide-hold-slide" test sequences, for velocity histories and environmental conditions employed in previous experiments. The modeling results capture all of the main features and trends seen in the experimental results, including both steady state and transient aspects of the observed behavior, with reasonable quantitative agreement. To our knowledge, ours is the first mechanism-based model that can reproduce RSF-like behavior in terms of microstructurally verifiable processes and state variables. Since it is microphysically based, we believe that our modeling approach can provide an improved framework for extrapolating friction data to natural conditions.

1. Introduction

Rock friction data have been widely used as input for modeling the dynamics of rupture nucleation, slip and healing associated with natural earthquakes and with induced seismicity. Such data are usually described using the so-called rate-and-state (RSF) friction law [*Dieterich*, 1979; *Ruina*, 1983], which expresses the rate (V) and state (θ) dependence of friction coefficient (μ), via the relation

$$\mu = \mu_0 + a\ln\left(\frac{V}{V^*}\right) + b\ln\left(\frac{V^*\theta}{D_c}\right) \tag{1}$$

where μ_0 is the steady state friction coefficient at a reference slip rate V^*, a and b are empirical (material) constants specifying the magnitude of the so-called "direct" and "evolution" effects that follow a stepwise increase in velocity from V^* to V, and D_c is the characteristic slip distance over which that evolution in μ takes place [*Dieterich*, 1979]. The dimensionless parameter (a-b) represents the difference in steady state friction values resulting from such a step in velocity and is thus used to describe the velocity dependence of fault frictional strength. Also embodied in the RSF constitutive framework is the concept that static fault restrengthening, following an active slip event, is expected to increase linearly with the logarithm of the healing or "hold" time [*Dieterich*, 1972, 1979], with the rate of restrengthening or healing (β) being expressed as

$$\beta = \frac{\partial\left(\Delta\mu_{\mathrm{pk}}\right)}{\partial \ln t_h} \tag{2}$$

where $\Delta\mu_{\mathrm{pk}}$ is the magnitude of frictional healing (the transient increase in frictional strength upon reshearing) and t_h is the hold time over which healing occurs.

These equations were developed to provide a phenomenological description of the frictional and healing behavior typically observed in lab experiments [*Dieterich*, 1979], the parameters contained within them being generally obtained simply by fitting the equations to curves obtained from velocity stepping or slide-hold-slide friction experiments [e.g., *Marone*, 1998b]. Though empirical in nature, it is widely agreed

that RSF laws somehow reflect competition between contact creep versus contact destruction within the relevant sliding interfaces [e.g., *Dieterich*, 1972]. In response to a reduced slip rate or to a stationary hold, the contact area within the sliding surfaces is expected to increase owing to creep of the existing contacts. When shearing switches to a faster rate or is resumed after a hold period, the contact area offers an increased resistance to shear due to a positive rate dependence of contact strength ("the direct effect"). After this transient response, the shear stress then evolves toward a new steady state value, corresponding to a new population of contacts ("the evolution effect") determined by the effects of contact growth versus destruction. This evolution can lead either to an increase in steady state strength with increasing sliding velocity (velocity strengthening) if the new contact population supports higher shear stress than the old or to a decrease in strength (velocity weakening) if lower shear stress is supported.

The above RSF laws are widely used to model natural faulting phenomena, including earthquake nucleation [e.g., *Scholz*, 2002], aftershock activity [*Marone et al*., 1995; *Chen and Lapusta*, 2009], slow slip [*Ampuero and Rubin*, 2008], and postseismic/interseismic fault creep and healing [*Marone*, 1998a; *Barbot et al*., 2009; *Hetland et al*., 2010]. However, there are several critical discrepancies between seismological constraints on RSF behavior associated with earthquakes and lab-derived RSF parameters, in particular, regarding the static stress drop and characteristic slip distance associated with seismic events [e.g., *Scholz*, 2002]. Moreover, lab friction studies can address only limited fault topographies, displacements, experimental durations and pressure-temperature (P-T) conditions, which means that scale issues, and especially processes like dilatation and fluid-rock interaction, cannot be fully taken into account. Without a basis for accounting for such effects, extrapolation of experimentally derived RSF data to nature, especially to coseismic slip, involves significant, often unknown, uncertainties.

Besides these difficulties, it has been long recognized that the RSF laws have shortcomings in reproducing laboratory results especially when extrapolating from one set of laboratory conditions to another [e.g., *Beeler et al*., 1994; *Chester*, 1994; *Marone et al*., 1995]. For instance, at hydrothermal conditions where fluid-assisted mass transfer processes are active, frictional healing may be strongly promoted, with the healing rates measured being far higher than the log-linear model used in RSF descriptions obtained at dry or room temperature conditions [*Karner et al*., 1997; *Nakatani and Scholz*, 2004; *Yasuhara et al*., 2005; *Niemeijer et al*., 2008]. One of the successes of RSF laws is that the rate dependence of steady state friction, typically expressed as (a-b), can be taken as an indicator of the potential of a fault to exhibit unstable versus stable slip. Numerical studies indicate that (a-b) or a/b are indeed key parameters in controlling both earthquake nucleation and rupture propagation [e.g., *Rice and Ruina*, 1983; *Tse and Rice*, 1986; *Rubin and Ampuero*, 2005]. However, experiments are increasingly showing that (a-b) is far from being a material constant and can change significantly not only with temperature but also with sliding rate, even in the low-velocity regime relevant to earthquake nucleation [*Shimamoto*, 1986; *Ikari et al*., 2009; *den Hartog and Spiers*, 2013; *Carpenter et al*., 2014; *Niemeijer et al*., 2016]. This rate dependence is not captured or explained by the classical concepts underlying the RSF laws. Hence, major uncertainties exist when taking (a-b) as an indicator of slip stability, especially considering the dynamic nature of rupture nucleation and load evolution on a tectonically active fault.

We believe that the deficiencies stated above are at least in part due to the fact that previous microphysical underpinning for RSF laws focus on sliding rock surfaces [*Dieterich*, 1979; *Baumberger et al*., 1999; *Nakatani*, 2001; *Rice et al*., 2001], that is based on a conceptual model of contact asperity growth and annihilation rather than on a description of the grain boundary sliding and dilatation/compaction processes observed to operate in fault gouges [e.g., *Sleep et al*., 2000; *Bos and Spiers*, 2002; *Niemeijer and Spiers*, 2006; *Noda*, 2008; *Mitsui and Ván*, 2014; *Ikari et al*., 2016]. In order to apply experimental results to natural fault zones more reliably, and, in particular, to extrapolate lab data beyond laboratory pressure, temperature, and velocity conditions, an understanding of the microphysical mechanisms governing fault frictional behavior is required. A better basis is needed to assess reliability and to underpin modeling of earthquake phenomenon and induced seismicity. Some earlier efforts have succeeded in predicting steady state frictional strengths of fault gouges, based on realistic, physical processes identified by means of microstructural analysis [*Bos and Spiers*, 2002; *Niemeijer and Spiers*, 2007; *den Hartog and Spiers*, 2014]. However, these models have, so far, addressed only steady state friction, with transient frictional behavior, i.e., the response to a perturbation in sliding rate, not yet being considered. An exception is the recent paper by *Noda* [2016], in which the model by *den Hartog and Spiers* [2014] is augmented by adding an RSF description of intergranular friction. This addition itself, however, has

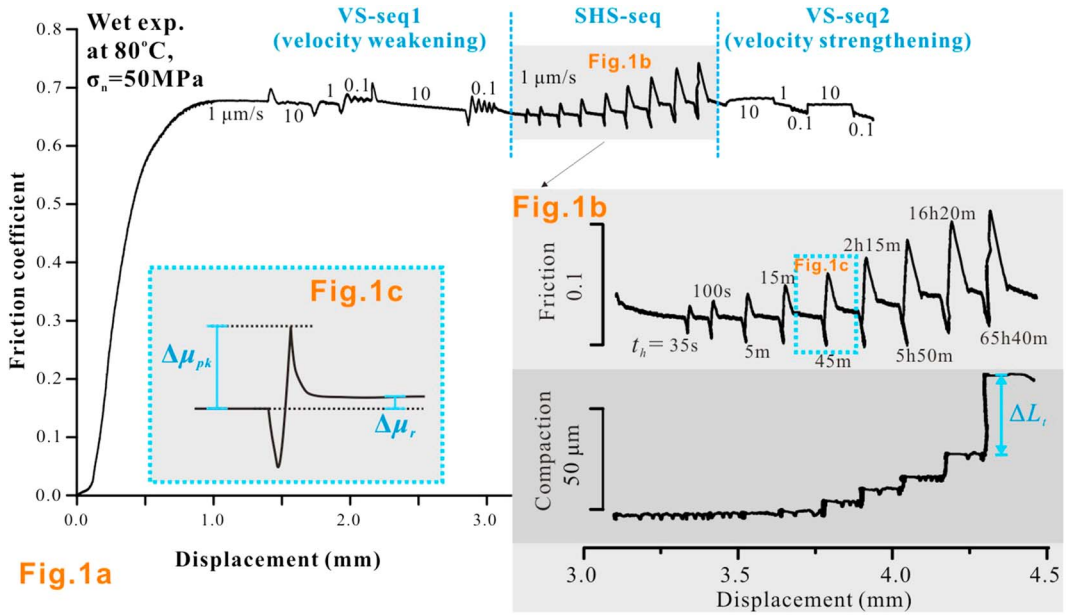

Figure 1. Representative experimental data on carbonate gouge sheared at hydrothermal conditions (compiled from *Chen et al.* [2015a]).

no microphysical basis but was introduced to avoid the ill posedness raised by purely rate-weakening friction. Ideally, of course, a single model based on the physical processes operating should be sought, which describes steady state, transient and healing behavior.

We recently reported frictional data on carbonate fault gouge [*Chen et al.*, 2015a] that demonstrate healing behavior characterized by a progressive increase in steady state friction after static hold periods. Similar behavior has been reported by *Yasuhara et al.* [2005] for quartz gouge and *Muhuri et al.* [2003] for gypsum gouge. This type of behavior cannot be explained by the transient healing effect embodied in classical RSF healing theory (equation (2)). Our experimental data and microstructural observations point to granular/cataclastic flow and pressure solution as the dominant deformation mechanisms, with slip localization occurring in boundary shears. Crystal plasticity may also play a role in the cataclastic grain size reduction process [*Verberne et al.*, 2013a, 2013b]. In the present paper, we develop a model for friction and healing that is based on the granular/cataclastic flow and pressure solution mechanisms. The modeled results capture all the main features of the frictional behavior observed in our lab experiments on carbonate gouge, as well as key aspects of the response expected using a classical RSF law. To the best of our knowledge, our model is the first friction model that is (a) based on a microphysical description of mechanisms inferred to operate via microstructural studies and (b) able to produce "RSF-like" behavior without resorting to the RSF equations.

2. Frictional Behavior of Carbonate Gouges Under Hydrothermal Conditions

We first summarize our previous friction experiments on carbonate fault gouge [*Chen et al.*, 2015a]. In that study, we employed a specially designed experimental strategy, consisting of sequential velocity stepping, slide-hold-slide (SHS) and velocity stepping" stages. The samples were sheared in a direct shear setup located in a triaxial testing machine at 20–140°C and 50 MPa (Terzaghi) effective normal stress. In experiments conducted wet, a fully drained (sample saturated) pore fluid pressure was maintained at 15 MPa throughout the experiments. As shown in Figure 1a, wet sample behavior at 80–140°C is characterized by macroscopic yield, giving way to steady state frictional sliding with $\mu_{ss} \approx 0.65$, plus unstable, velocity-weakening behavior in the first velocity stepping sequence (VS-1). Subsequent SHS testing is characterized by a transient peak healing effect ($\Delta\mu_{pk}$) but also by a permanent increase in steady state friction, referred to as the persistent strengthening ($\Delta\mu_r$) (Figure 1c). A pronounced increase in (a-b) can be seen in the second VS sequence (VS-2) after the SHS stage, leading, at 80°C and above to a transition from velocity weakening (seen in VS-seq1) to velocity

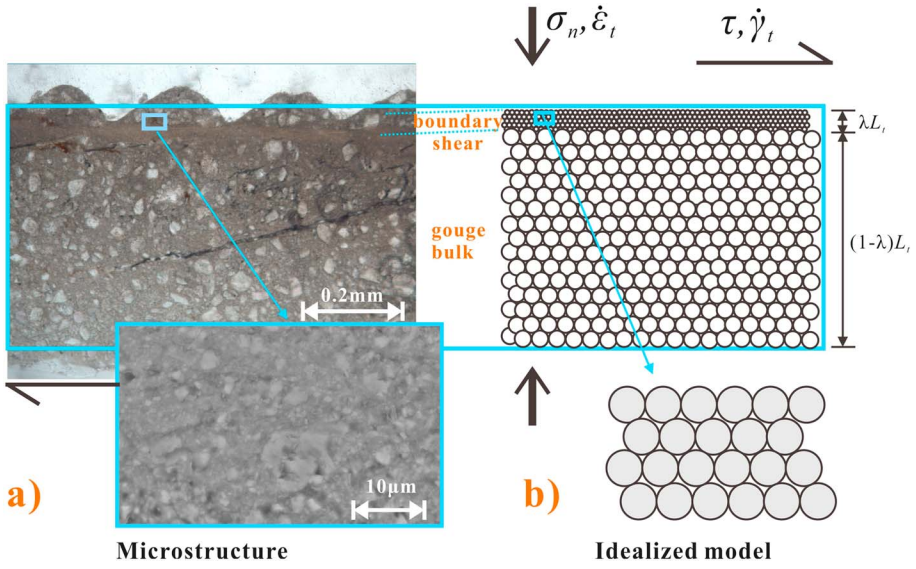

Figure 2. (a) Representative microstructure of experimentally sheared carbonate gouge samples [*Verberne et al*., 2013b; *Chen et al*., 2015a] and (b) the idealized microstructural model employed here. Note the impression of the tooth grips in the top surface of the experimentally sheared sample, immediately above the highly localized boundary shear in Figure 2a.

strengthening (seen in VS-seq2). All of these features were absent in identical tests performed on dry samples. In the following, we focus on the results for wet samples.

Based on the microstructural observations and enhanced gouge compaction seen in wet versus dry samples [*Chen et al*., 2015a], intergranular pressure solution (IPS) was inferred to be an important deformation mechanism in our experiments. As shown in Figure 1b, marked gouge compaction was observed especially during the longer hold periods. Mean compaction strain rates calculated over such periods displayed a negative temperature dependence [*Chen et al*., 2015b], in line with the decrease in solubility of calcite seen with increasing temperature and suggesting that grain boundary diffusion is the process controlling the rate of IPS [*Liteanu et al*., 2012]. The postdeformational gouge microstructure also revealed a well-developed cataclasite signature in both the bulk gouge and prominently developed boundary shears (Figure 2), indicating that brittle grain failure and granular flow were probably the most important shearing mechanisms in our experiments. For detailed mechanical data and an analysis of the active deformation mechanisms, see *Chen et al*. [2015a].

3. Microphysical Model Development

To develop a microphysical model, we start by constructing a microstructural model, based on the microstructure observed in our experiments on carbonate gouge, and by defining related microstructural state variables (i.e., porosity, average grain contact area, and dilatancy angle). We proceed to derive a kinematic equation linking sample deformation/slip, machine distortion, and imposed displacement at the "load point" (i.e., at the conceptual point of application of shear load to the apparatus or loading frame). Using an energy/entropy balance approach, we subsequently establish a second equation relating shear stress evolution to changing microstructure. Coupling these equations with an atomic to nanometer-scale model for rate-strengthening grain boundary sliding friction leads to our final microphysical model, describing the frictional behavior of a granular fault gouge in response to any boundary condition imposed on it, including constant velocity sliding, velocity stepping, SHS testing or fixed boundary stresses.

3.1. Idealized Microstructural Model

Figure 2a shows a representative example of the microstructure exhibited by a wet carbonate gouge sheared at 80–140°C and 50 MPa effective normal stress. A fine-grained boundary shear zone measuring 20–40 μm in thickness is clearly developed at the upper sample interface [see also *Verberne et al*., 2013b; *Chen et al*., 2015a]. The bulk of the gouge layer is less deformed and shows a chaotic microstructure, with a particle size distribution similar to the starting material (average grain size 28 μm). Inclined Riedel shear bands (R1 shears,

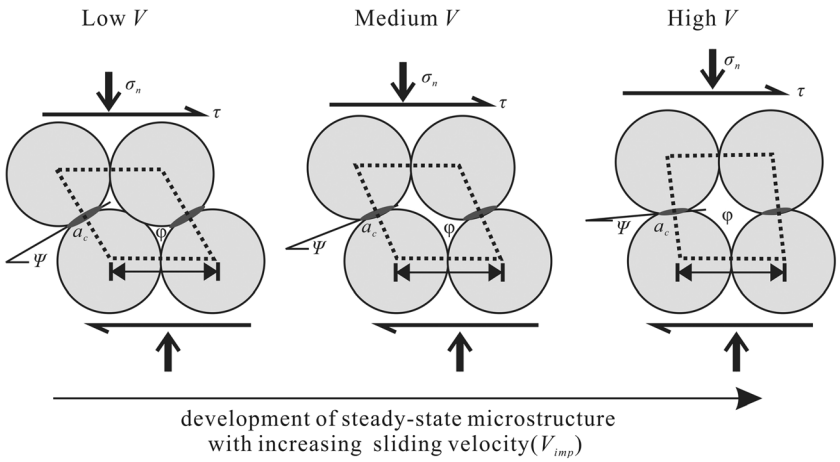

Figure 3. Conceptual model illustrating the evolution of the key microstructural state variables, i.e., dilatancy angle (ψ), porosity (φ), and average contact area (a_c), with increasing sliding velocity (V_{imp}).

following the terminology of *Logan et al.* [1992]) can also be discerned locally. The boundary shear is characterized by extreme grain size reduction compared with the gouge bulk. Particles within this boundary shear band are poorly distinguishable with an optical microscope. However, scanning electron microscope images show a chaotic, granular microstructure similar to the gouge bulk, with grain sizes mainly in the range of 0.1–5 μm (Figure 2a) [see also *Verberne et al.*, 2014]. On basis of the observed microstructure, we adopt the idealized microstructural model shown in Figure 2b, featuring a localized shear band developed at the margin of the bulk gouge. Both gouge zones are represented by densely packed cylinders or spheres, with different mean diameters per zone, representing the constituent grains [*Niemeijer and Spiers*, 2007]. Imposed shear displacement is assumed to be accommodated mostly by the localized shear band, as observed in our experiments [*Verberne et al.*, 2013b; *Chen et al.*, 2015a]. The thickness of the shear band is defined as λL_t, where L_t is the total thickness of the gouge layer and λ is taken as a constant defining relative shear band thickness ($\lambda \leq 1$).

3.2. Microstructural State Variables and Associated Relationships

Following the approach used by *Niemeijer and Spiers* [2007], shear deformation of both gouge zones is assumed to occur predominantly by granular flow with grain neighbor swapping occurring as grains slide over each other. We accordingly assume that there is no contribution by grain fracturing such that the grain size remains constant. Slip occurs on the inclined grain contacts, leading to dilatation with a dilatancy angle (ψ) [*Paterson*, 1995]. Intergranular pressure solution (IPS) also occurs at grain contacts (each of area a_c), in response to the stresses transmitted across them, causing thermally activated (rate-dependent) deformation in both the normal and shear directions. We assume that grains do not roll but slide over each other (on truncated pressure solution surfaces). Figure 3 shows snapshots of the evolution of the microstructural model with increasing imposed sliding velocity. With increasing shear rate, ψ becomes progressively smaller as dilatation becomes increasingly dominant over compaction by pressure solution, generating higher porosity φ and lower grain contact area a_c.

The microstructural state of the gouge material, in both gouge zones represented in Figure 2, is thus controlled by competition between compaction by IPS and dilatation due to granular flow. As explained by *Niemeijer and Spiers* [2007], this microstructural model is reasonable provided that competition between compaction and dilatation ensures that the porosity remains below the maximum attainable (critical state) value.

To quantify the rate of change of volume due to the combined effects of granular flow and IPS during shearing and/or static healing, relations are required that link the above state variables, i.e., ψ, φ, and a_c. Clearly, for any given grain packing geometry (e.g., a cubic pack of spherical grains of diameter d), ψ, a_c, and φ are interdependent on one another (Figures 3 and 4). Following *Niemeijer and Spiers* [2007], ψ can be adequately related to φ by a function of the form

$$\tan\psi \approx H(q - 2\varphi) \tag{3}$$

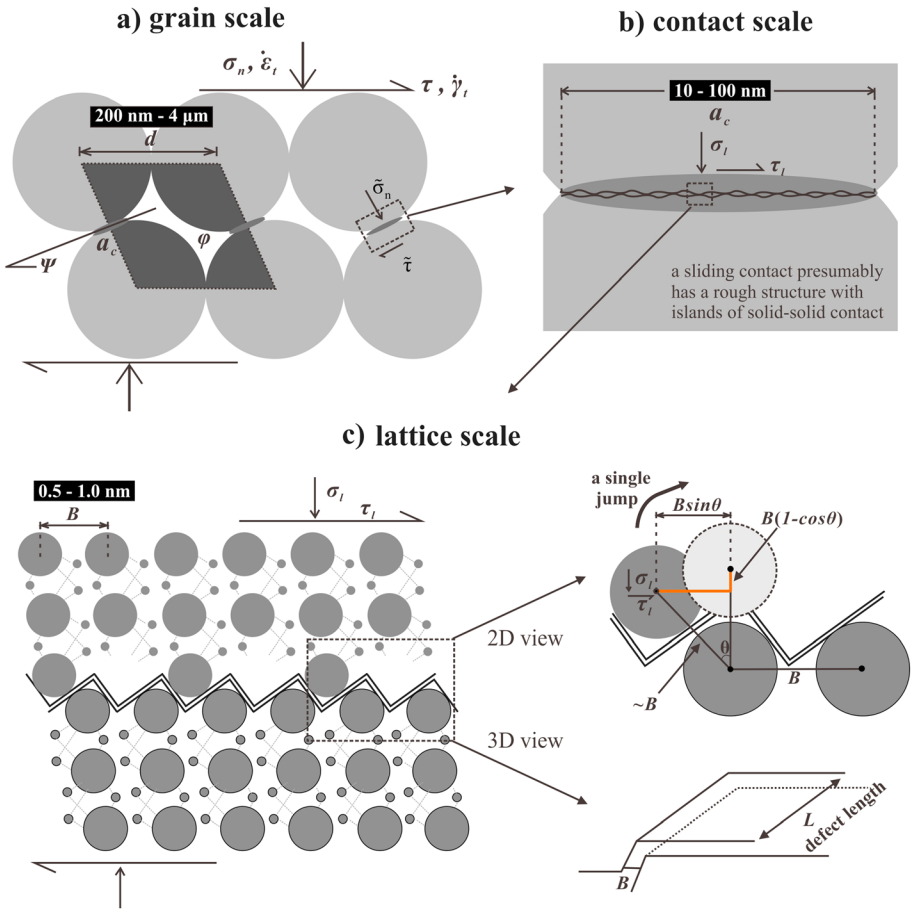

Figure 4. Schematic models showing grain contacts at the various scales considered in the present model development. (a) The unit cell characterizing the grain pack in the present microstructural model; (b) schematic representation of a single contact that consists of many small-scale solid-solid islands or contact points; and (c) 2-D and 3-D models showing that the interaction of lattices in the atomic scale during the grain contact sliding process. Grain diameter is d, and grain-to-grain contact area per unit cell is $a_c = 2 \times \frac{1}{2}\, a_c$. The atoms with large and small diameters in Figure 4c schematically represent anions and cations in the lattice, respectively. See definitions and values for the parameters marked in text.

where H and q are geometric constants, with H lying in the range $1/\sqrt{3}$ to $\sqrt{3}$ for a 2-D grain pack, and q being 2 times the critical state porosity φ_c for granular flow, which when $\varphi = \varphi_c$ yields the extreme case that tan ψ equals zero. This function describes a monotonic decrease in ψ with increasing φ, in line with that observed during purely granular flow of particulate materials with a porosity less than the critical state value [e.g., *Campbell*, 2006]. To describe how the mean grain-to-grain contact area a_c depends on φ, we assume that a_c is related to the surface area of a spherical grain via the average coordination number z and gouge porosity φ such that $a_c = \pi d^2/z\ f(\varphi)$, where d is grain diameter (Figure 4) [*Spiers et al.*, 2004]. For this relation to be accurate, the porosity function $f(\varphi)$ needs to be chosen such that (i) $f(\varphi) \rightarrow 1$ when $\varphi \rightarrow 0$ and (ii) $f(\varphi) \rightarrow 0$ as $\varphi \rightarrow \varphi_c$ (so that contacts possess negligible contact area when $\varphi = \varphi_c$) [*Pluymakers and Spiers*, 2014]. Analysis of the geometry of a simple cubic, or body-centered cubic pack of initially spherical grains compacted isotropically by pressure solution [*Renard et al.*, 1999; *Niemeijer et al.*, 2002], shows that the relation between contact area and porosity is well approximated using $f(\varphi) = (q - 2\varphi)$ and hence by the relation

$$a_c = \pi d^2 (q - 2\varphi)/z \tag{4}$$

for porosities from ~40% down to ~5%. Note, however, that equation (4) does not satisfy the condition that $a_c = \pi d^2/z$ when $\varphi \rightarrow 0$, so that another function is required at porosities lower than ~5% [*Pluymakers and Spiers*, 2014]. We use equation (4) here assuming that this relation holds for gouge material undergoing deformation in both the normal and shear directions, at porosities $> 5\%$. Hence, using (3) and (4), both a_c and ψ can be related to the key microstructural state variable φ.

3.3. Kinematic Relations for Gouge Deformation

3.3.1. Normal and Shear Strain Rate Components

In this analysis, we assume both the gouge bulk and boundary shear band deforms by two parallel processes, i.e., granular flow and pressure solution. Elastic deformation of the gouge is neglected. This allows us to write normal and shear strain rates ($\dot{\varepsilon}_t$ and $\dot{\gamma}_t$) in any representative volume of gouge as

$$\dot{\varepsilon}_t = \dot{\varepsilon}_{ps} + \dot{\varepsilon}_{gr} \tag{5a}$$

$$\dot{\gamma}_t = \dot{\gamma}_{ps} + \dot{\gamma}_{gr} \tag{5b}$$

Here compaction is taken as positive $\dot{\varepsilon}_t$, the subscript "t" indicates measured, total shear or compaction strain rate, and "ps" and "gr" represent deformation attributed to pressure solution and granular flow, respectively. Considering that compaction and shear deformation occur both within and outside the shear band (Figure 2), we further have

$$\dot{\varepsilon}_{ps} = \lambda\dot{\varepsilon}_{ps}^{sb} + (1-\lambda)\dot{\varepsilon}_{ps}^{bulk} \tag{6a}$$

$$\dot{\gamma}_{ps} = \lambda\dot{\gamma}_{ps}^{sb} + (1-\lambda)\dot{\gamma}_{ps}^{bulk} \tag{6b}$$

where the superscripts sb and bulk indicate the shear band and remaining bulk gouge, respectively. Since shearing is concentrated in the shear band, we assume that significant granular flow and dilation only occur in the shear band, so that $\dot{\varepsilon}_{gr}^{bulk} = 0$ and $\dot{\gamma}_{gr}^{bulk} = 0$. Following the classical soil mechanics approach to granular flow [*Paterson*, 1995], dilatation due to granular flow in the shear band can be described using the relation $\dot{\varepsilon}_{gr}^{sb} = -(\tan\psi)\dot{\gamma}_{gr}^{sb}$. Using these relations, the compaction strain rate within the shear band, the bulk, and entire gouge layer (bulk plus shear band) can hence be written as

$$\dot{\varepsilon}_t^{sb} = \dot{\varepsilon}_{ps}^{sb} - (\tan\psi)\dot{\gamma}_{gr}^{sb} \tag{7a}$$

$$\dot{\varepsilon}_t^{bulk} = \dot{\varepsilon}_{ps}^{bulk} \tag{7b}$$

$$\dot{\varepsilon}_t = \lambda\dot{\varepsilon}_{ps}^{sb} + (1-\lambda)\dot{\varepsilon}_{ps}^{bulk} - \lambda(\tan\psi)\dot{\gamma}_{gr}^{sb} \tag{7c}$$

Similarly, the shear strain rate within the shear band, the bulk, and entire gouge layer are given as

$$\dot{\gamma}_t^{sb} = \dot{\gamma}_{ps}^{sb} + \dot{\gamma}_{gr}^{sb} \tag{8a}$$

$$\dot{\gamma}_t^{bulk} = \dot{\gamma}_{ps}^{bulk} \tag{8b}$$

$$\dot{\gamma}_t = \lambda\dot{\gamma}_{ps}^{sb} + (1-\lambda)\dot{\gamma}_{ps}^{bulk} + \lambda\dot{\gamma}_{gr}^{sb} \tag{8c}$$

3.3.2. Rate of Compaction/Dilatation

To quantify the transient evolution of gouge layer porosity and strength in response to deformation, we now need a relation linking porosity of the material (φ) to normal strain rate ($\dot{\varepsilon}$). Assuming a closed elementary volume of gouge material with respect to solid species mass and volume, then the solid volume (V_s) will be constant at all times. The dynamic porosity is therefore related to the total volume of the gouge (V) via $\varphi = 1 - V_s/V$. The time derivative of this then yields

$$\dot{\varphi} = \frac{V_s\dot{V}}{V^2} = \frac{(1-\varphi)\dot{V}}{V} \tag{9a}$$

Here $\dot{V}/V$ is the volumetric strain rate measured in terms of dilatation normal to the shear plane. This is equal to the compaction strain rate but with the opposite sign, such that $\dot{\varepsilon} = -\dot{V}/V$. Hence, (9a) becomes

$$\dot{\varphi} = -(1-\varphi)\dot{\varepsilon} \tag{9b}$$

Allowing now for dilatation and/or compaction to occur both within a boundary shear band and within the remainder of a bulk gouge layer, the porosity within the shear band (φ^{sb}) and the bulk gouge layer (φ^{bulk}) can be expressed as

$$\dot{\varphi}^{sb} = -\left(1-\varphi^{sb}\right)\dot{\varepsilon}_t^{sb} \tag{10a}$$

$$\dot{\varphi}^{bulk} = -\left(1-\varphi^{bulk}\right)\dot{\varepsilon}_t^{bulk} \tag{10b}$$

By introducing (7a) into (10a), the dynamic porosity of the shear band can in turn be expressed as

$$\dot{\varphi}^{sb}/\left(1-\varphi^{sb}\right) = (\tan\psi)\dot{\gamma}_{gr}^{sb} - \dot{\varepsilon}_{ps}^{sb} \tag{11}$$

3.3.3. Relationship Between Gouge Shearing Rate and Load Point Velocity

To relate the instantaneous shear strain rate of the entire gouge layer $(\dot{\gamma}_t)$ to the shear velocity imposed upon the loading system (V_{imp}), it is critical to note that V_{imp} is accommodated by (dynamic) elastic deformation of the loading system and by deformation of the sample. This relation can be expressed as

$$V_{imp} = V_{el} + \dot{\gamma}_t L_t \tag{12}$$

where V_{el} is the velocity due to elastic machine distortion caused by change in shear stress, given as

$$V_{el} = \dot{\tau}/K \tag{13}$$

Here K is the stiffness of the loading system, and $\dot{\tau}$ is the time derivative of shear stress. In this equation, we neglect the elastic deformation of the gouge as well as the inertial term.

Combining equations (8c), (12), and (13) now yields the equation linking the imposed load point velocity, machine distortion rate, and sample deformation rate as follows

$$V_{imp} - \dot{\tau}/K = L_t\left[\lambda\dot{\gamma}_{ps}^{sb} + (1-\lambda)\dot{\gamma}_{ps}^{bulk}\right] + L_t\lambda\dot{\gamma}_{gr}^{sb} \tag{14}$$

3.4. Energy Balance and Dynamic Gouge Strength

To formulate relations for the frictional resistance to sliding and the deformation rate accommodated by intergranular pressure solution at grain contacts, in either a boundary shear or bulk gouge layer, we need to quantify the stresses supported at grain-to-grain contacts. This can be easily done with reference to the unit cell that describes (average) grain packing shown in Figure 4a. For given externally applied effective normal and shear stresses (σ_n and τ), the horizontal and vertical forces on the unit cell are $F_h = \tau d^2$ and $F_v = \sigma_n d^2$, respectively. The force transmitted across grain contacts then requires that the intensified effective normal and shear stresses acting on the contacts $(\widetilde{\sigma}_n,\ \widetilde{\tau})$ are given by the relations

$$\widetilde{\sigma}_n = \left(\sigma_n d^2\cos\psi + \tau d^2\sin\psi\right)/a_c \tag{15a}$$

$$\widetilde{\tau} = \left(\tau d^2\cos\psi - \sigma_n d^2\sin\psi\right)/a_c \tag{15b}$$

Now following *Lehner* [1990] [see also *Lehner and Bataille*, 1984], the combined energy/entropy balance plus the second law of thermodynamics for unit volume of fault gouge undergoing direct shear deformation can be written as

$$\tau\dot{\gamma}_t + \sigma_n\dot{\varepsilon}_t - \dot{f} = \dot{\Delta} = T\Gamma \geq 0 \tag{16}$$

where $\dot{f}$ is the rate of change in Helmholtz free energy of the solid phase per unit volume of the gouge, $\dot{\Delta} = T\Gamma$ is the total dissipation per unit volume caused by the irreversible microscale processes operating, T is absolute temperature and Γ is the total rate of internal entropy production. This equation (16) simply states that the work done by mechanical deformation (first two terms), minus the free energy stored in the solid framework $\left(\dot{f}\right)$, is dissipated irreversibly as heat $\left(\dot{\Delta} = T\Gamma\right)$, with the inequality expressing this irreversibility via the second law ($T\Gamma \geq 0$). As a first approximation, it is reasonable to suppose that $\dot{f} \approx 0$, since frictional shear stress changes typically associated with changes in slip velocity will generally cause negligible changes in the thermodynamic state (elastic or defect-stored energy) of the solid, though we note that extreme grain size reduction (surface area increase) through cataclasis may cause changes in f that cannot be neglected. If the gouge deforms by frictional granular flow plus pressure solution, then assuming negligible $\dot{f}$ and negligible dissipation due to viscous flow of the pore fluid phase compared to deformation of the gouge framework, the preinequality part of (16) can be rewritten as

$$\tau\dot{\gamma}_t + \sigma_n\dot{\varepsilon}_t = \dot{D}_{gr} + \dot{D}_{ps}^{comp} + \dot{D}_{ps}^{shear} \tag{17}$$

where $\dot{D}_{gr}$ is the dissipation or energy release rate due to frictional sliding on grain contacts and $\dot{D}_{ps}^{comp}$ and $\dot{D}_{ps}^{shear}$ represent dissipation due to deformation by IPS normal and parallel to the shear plane, respectively. Following *Niemeijer and Spiers* [2007], the dissipation due to contact friction can be written as $\dot{D}_{gr} = \dot{\Delta}_c N_c$, where $\dot{\Delta}_c = \widetilde{\tau} a_c \widetilde{v}_c$ is the dissipation rate per sliding contact, N_c is the number of contacts per unit volume of the deforming fault gouge, and $\widetilde{v}_c$ is the average slip rate on the contacts. From the unit cell geometry

(Figure 4a), it is apparent that $N_c = 1/(d^3 \cos\psi)$. Also from the cell geometry, the horizontal shear displacement rate due to intergranular sliding, measured across the unit cell, can be written as $V_{gr} = h\dot{\gamma}_{gr} \approx (d\cos\psi)\dot{\gamma}_{gr}$, where h is the height of the unit cell, while the average slip rate on the contacts can be written as $\tilde{v}_c = V_{gr}/\cos\psi = d\dot{\gamma}_{gr}$. Hence, the dissipation by granular flow is given as

$$\dot{D}_{gr} = \frac{\tilde{\tau} a_c \dot{\gamma}_{gr}}{d^2 \cos\psi} \tag{18a}$$

The stresses acting on individual contacts must satisfy a grain boundary slip criterion, which we assume to be of Coulomb type given $\tilde{\tau} = \tilde{\mu}\tilde{\sigma}_n + \tilde{c}$, where $\tilde{\mu}$ is the intrinsic friction coefficient for contact sliding and $\tilde{c}$ is the cohesive strength of contacts. Using the cohesion-free slip criterion for each contact $(\tilde{\tau} = \tilde{\mu}\tilde{\sigma}_n)$ and force transmission relation (15b), we now get

$$\dot{D}_{gr} = \tilde{\mu}\sigma_n\dot{\gamma}_{gr} + \tilde{\mu}\tau(\tan\psi)\dot{\gamma}_{gr} \tag{18b}$$

Assuming that all mechanical work done in causing deformation by pressure solution is fully dissipated through the microscale processes of mass dissolution, grain boundary diffusion and precipitation, and that the gouge deforms as an isotropic material, we can also write

$$\dot{D}_{ps}^{comp} = \sigma_n\dot{\varepsilon}_{ps} \quad \text{and} \quad \dot{D}_{ps}^{shear} = \tau\dot{\gamma}_{ps} \tag{19}$$

Substituting (18b) and (19) into (17) now yields

$$\tau\dot{\gamma}_t + \sigma_n\dot{\varepsilon}_t = \tilde{\mu}\sigma_n\dot{\gamma}_{gr} + \tilde{\mu}\tau(\tan\psi)\dot{\gamma}_{gr} + \sigma_n\dot{\varepsilon}_{ps} + \tau\dot{\gamma}_{ps} \tag{20}$$

where, by virtue of (16), the right-hand side = $T\Gamma \geq 0$. Using the kinematic relation in the shear direction (5b), i.e., the relation $\dot{\gamma}_t = \dot{\gamma}_{ps} + \dot{\gamma}_{gr}$, equation (19) can now be rewritten as

$$\tau\dot{\gamma}_{gr}(1 - \tilde{\mu}\tan\psi) + \sigma_n\dot{\varepsilon}_t = \sigma_n\tilde{\mu}\dot{\gamma}_{gr} + \sigma_n\dot{\varepsilon}_{ps} \tag{21}$$

Similarly, using the kinematic relation in the normal direction (5a), namely, $\dot{\varepsilon}_t = \dot{\varepsilon}_{ps} + \dot{\varepsilon}_{gr}$, equation (20) can be further reduced to

$$\tau = \frac{\tilde{\mu} + \tan\psi}{1 - \tilde{\mu}\tan\psi}\sigma_n \tag{22}$$

This "friction law," obtained from the energy balance approach, holds at all times for a granular fault gouge. Note that in deriving it we have neglected dissipative processes associated with grain fracturing and elastic wave radiation, as well as kinetic energy changes related to inertial effects. Work terms related to dilatation/compaction associated with slip de/localization have also been neglected (λ is assumed constant). Interestingly, the result is identical to that obtained by *Niemeijer and Spiers* [2007] using a stress balance approach. Like their equation (19), equation (21) demonstrates that the frictional strength of a granular fault gouge is determined by the grain boundary friction $(\tilde{\mu})$ and the microstructural state of the gouge, specifically the dilatation angle (ψ) and hence porosity (φ). However, the present derivation of (21) also makes clear that the state of the gouge (ψ) is determined by pressure solution operating in competition with dilatant intergranular sliding.

3.5. Rate-Strengthening Grain Boundary Friction

Previous microphysical modeling work following the above approach has assumed $\tilde{\mu}$ to be a constant. This means that equation (21) predicts steady state frictional behavior for given steady state values of porosity, and dilatancy angle, achieved when dilatation due to granular flow, is balanced by compaction due to pressure solution [*Niemeijer and Spiers*, 2007]. It also predicts an evolution effect when porosity and dilatancy angle change due to a change in sliding velocity. For a stepwise increase in velocity from an initial steady state, this evolution consists of a drop in frictional strength caused by dilatation due to granular flow transiently outstripping compaction by pressure solution. It proceeds until the porosity, and hence, pressure solution rate becomes so high that the balance between dilatation and compaction is reestablished at a new, lower steady state friction level [*Niemeijer and Spiers*, 2007]. However, in sharp contrast to most experiments, including our previous work on carbonate fault gouge [*Chen et al.*, 2015a], no direct effect is predicted when the grain boundary friction $\tilde{\mu}$ is assumed constant [see *Noda*, 2016].

Significantly, a consensus has emerged in the past decade that grain boundary friction can be described as logarithmically dependent on shear velocity, reflecting the operation of a thermally activated defect glide or creep process at asperity contacts within grain boundaries [e.g., *Tullis and Weeks*, 1987; *Beeler et al*., 1996; *Nakatani*, 2001; *Rice et al*., 2001]. Such a process operating within sliding grain contacts will impart a direct effect to $\widetilde{\mu}$ and hence to τ via equation (21). However, the mechanistic and theoretical basis for such a process remains unclear. In the following, we revisit the grain boundary shearing process, for the case of intergranular sliding in a calcite gouge, analyzing it at the atomic to nanometer scale.

Based on the porous microstructure of the shear band developed in our carbonate fault gouge samples, the contact area of adjacent grains participating in a granular flow process will be much smaller than the cross section of the grains themselves (cf. Figures 4a and 4b). If the grains are micron sized, the grain contacts will be tens or at most hundreds of nanometers in diameter. Such a sliding contact will presumably have a rough structure with islands of solid-solid contact (Figure 4b). Interacting "asperities" within such islands will ultimately be at the lattice step or atomic scale and will likely be coated with adsorbed species such as water. Frictional resistance to sliding on grain contacts at this scale must accordingly involve interactions on a length scale about equal to the lattice spacing B (Figure 4c). At this scale, conventional asperity creep models for contact friction [e.g., *Baumberger et al*., 1999; *Berthoud et al*., 1999; *Nakatani*, 2001] cannot be expected to apply.

To develop a model for grain boundary friction, we assume that the above interactions can be considered as barriers to atomic scale jumps, or to defect motion, in contact zones of only a few atoms or tens of atoms, and that an individual atomic or defect scale jump allows a sliding displacement increment equal (or proportional) to the lattice spacing B. From the balance of shear and normal forces transmitted across contacts at the grain scale and at the internal island/asperity or lattice contact scale, it is easily shown that the grain boundary friction coefficient defined $\widetilde{\mu} = \widetilde{\tau}/\widetilde{\sigma}_n$ is independent of true load supporting contact area and is equal to τ_l/σ_l where τ_l and σ_l are the shear and normal stresses supported at the lattice contact scale [see also *Rice et al*., 2001]. We now further assume that the elementary atomic or defect scale jump enabling lattice contact sliding is characterized by a maximum energy barrier at zero normal stress of ΔF. Under the action of a normal stress σ_l and a shear stress τ_l at the lattice contact scale, this barrier will be modified by the mechanical work terms associated with achieving both the normal and shear displacements involved in the elementary jump transition. The energy barrier in the stressed state is accordingly given as

$$\Delta\Phi = \Delta F + \sigma_l LB^2(1-\cos\theta) - \tau_l LB^2\sin\theta \tag{23}$$

where L, B, and θ are geometric parameters associated with the barrier to lattice contact sliding, as defined in Figure 4c. Here the second and third terms on the right, respectively, represent the normal and shear work terms associated with the jump transition state. Employing the standard statistical mechanics approach, the forward jump frequency with which the barrier to lattice contact sliding is overcome can now be expressed as

$$f_+ = \upsilon\cdot\exp\left[-\frac{\Delta F + \sigma_l LB^2(1-\cos\theta) - \tau_l LB^2\sin\theta}{kT}\right] \tag{24a}$$

where υ is the lattice vibration frequency, k the Boltzmann constant, and T the absolute temperature. The exponential term in (23) expresses the jump success possibility, which for the forward jump is promoted by the local shear stress τ_l. Conversely, the reverse jump frequency takes the form

$$f_- = \upsilon\cdot\exp\left[-\frac{\Delta F + \sigma_l LB^2(1-\cos\theta) + \tau_l LB^2\sin\theta}{kT}\right] \tag{24b}$$

whereby the jump process is impeded by τ_l. The resulting net jump frequency is

$$f_R = f_+ - f_- = 2\upsilon\cdot\exp\left[-\frac{\Delta F + \sigma_l LB^2(1-\cos\theta)}{kT}\right]\sinh\left(\frac{\tau_l LB^2\sin\theta}{kT}\right) \tag{24c}$$

Therefore, assuming a jump distance B, the velocity of lattice contact sliding ($\widetilde{v}_c$) by direct jumping or by migration of a contact defect is

$$\widetilde{v}_c = Bf_R = 2B\upsilon\cdot\exp\left[-\frac{\Delta F + \sigma_l LB^2(1-\cos\theta)}{kT}\right]\sinh\left(\frac{\tau_l LB^2\sin\theta}{kT}\right) \tag{25}$$

Taking logarithm of this equation leads to a full expression for the frictional coefficient describing the grain boundary sliding [*Rice et al*., 2001] (see supporting information).

Consider, now, a contact velocity step from a reference value $\widetilde{v}_c^*$ to $\widetilde{v}_c$. From (24c), we have

$$\widetilde{v}_c^* = 2B\upsilon\cdot\exp\left[-\frac{\Delta F + \sigma_l LB^2(1-\cos\theta)}{kT}\right]\sinh\left(\frac{\tau_l^* LB^2\sin\theta}{kT}\right) \tag{26a}$$

where τ_l^* represents the shear stress supported at the lattice contact scale at the reference velocity $\widetilde{v}_c^*$. Dividing (25) over (24c) gives

$$\frac{\widetilde{v}_c}{\widetilde{v}_c^*} = \frac{\sinh\left[\tau_l LB^2\sin\theta/(kT)\right]}{\sinh\left[\tau_l^* LB^2\sin\theta/(kT)\right]} \tag{26b}$$

If the reverse jump frequency f_- in (24a) is zero, due to wide barrier spacing, or if $\tau_l LB^2\sin\theta >> kT$ (see details in the supporting information), the hyperbolic sine functions in (26a) reduce to the exponential form, which upon taking logarithms yields

$$\ln\left(\frac{\widetilde{v}_c}{\widetilde{v}_c^*}\right) = \frac{(\tau_l - \tau_l^*)kT}{LB^2\sin\theta} \tag{27a}$$

The change in lattice-scale shear stress (shear resistance) at velocity $\widetilde{v}_c$ relative to a reference velocity $\widetilde{v}_c^*$ can thus be described as

$$\tau_l - \tau_l^* = \frac{kT}{LB^2\sin\theta}\ln\left(\frac{\widetilde{v}_c}{\widetilde{v}_c^*}\right) \tag{27b}$$

By virtue of the definition $\widetilde{\mu} = \tau_l/\sigma_l$ and the fact that $\widetilde{v}_c = V_{gr}/\cos\psi = d\dot{\gamma}_{gr}$ (see derivation of equation (18a)), the rate-dependent grain boundary friction $\widetilde{\mu}$ can be expressed in terms of shear strain rate as

$$\widetilde{\mu} = \widetilde{\mu}^* + a_{\widetilde{\mu}}\ln\left(\frac{\dot{\gamma}}{\dot{\gamma}^*}\right) \tag{28}$$

where $\widetilde{\mu}^*$ is the reference grain boundary friction at a reference strain rate $\dot{\gamma}^*$ and $a_{\widetilde{\mu}} = kT/\left(\sigma_l LB^2\sin\theta\right)$ is a rate-dependent coefficient constituting a direct effect in RSF terminology. Equation (27b) implies that grain boundary friction will show rate-strengthening behavior and a direct effect that increases proportionally with absolute temperature.

Taking $LB^2\sin\theta$ as the activation volume Ω for the atomic scale jump process, (27b) is seen to be identical in form to relations for grain contact friction obtained in previous conceptual models [e.g., *Nakatani*, 2001; *Rice et al*., 2001]. In previous analyses, however, contact asperity shear strength has been assumed to be controlled by an asperity creep law equivalent to a macroscopic dislocation glide flow law, neglecting any effect of contact normal stress on the energy barrier for glide. Given the extremely small scale of the lattice contact points within submicrometer-sized grain contacts observed in our experiments on calcite gouge [*Chen et al*., 2015a, 2015b], we believe that the present analysis, which allows for the effect of contact-normal displacements and associated mechanical work on the elementary energy barrier for contact sliding, is physically more realistic. In previous models of contact asperity friction assuming macroscopic creep behavior of asperity contacts, an evolution effect is generally incorporated, alongside a direct effect similar to that seen in (27b), by allowing for dynamic competition between contact elimination, recreation, and spreading by contact-normal creep [e.g., *Dieterich*, 1979; *Berthoud et al*., 1999; *Nakatani*, 2001; *Rice et al*., 2001]. At the atomic step scale of our model for grain contact friction, we assume that the surface topography and population of lattice contact points will be controlled by the combined processes of pressure solution and grain neighbor swapping, which will ensure that sliding grain contact surfaces remain rough at the atomic scale with little sensitivity to contact sliding velocity. Our model accordingly predicts only velocity-strengthening behavior of grain contacts, with the grain contact friction coefficient $\widetilde{\mu}$ being given by equation (27b). This in turn imparts a direct effect into our overall model.

3.6. Rate of Normal and Shear Deformation by IPS

Numerous authors [e.g., *Rutter*, 1976, 1983; *Raj and Chyung*, 1981; *Lehner*, 1990; *Shimizu*, 1995; *Spiers et al*., 2004; *Pluymakers and Spiers*, 2014] have published theoretically derived rate equations for both deviatoric

and compaction creep by IPS. Here we assume that the gouge behaves like an isotropic material with respect to IPS, so that the effects of σ_n and τ on compaction and shear deformation can be treated separately [cf. *Raj and Chyung*, 1981]. Against this background, compaction of the gouge normal to the shear plane can be modeled using a standard 1-D or uniaxial creep law for a regular pack of spherical grains [e.g., *De Meer and Spiers*, 1997; *Spiers et al*., 2004]. Assuming grain boundary diffusion controlled IPS, as reported in compaction experiments on calcite by *Zhang et al*. [2010], the normal compaction strain rate under the effective normal stress σ_n can hence be expressed as

$$\dot{\varepsilon}_{ps} = A_d \frac{DCS}{d^3} \frac{\sigma_n \Omega}{RT} f_d(\varphi) \tag{29}$$

Here A_d is a geometric constant, D is the diffusivity of the dissolved solid within the grain boundary fluid (m^2/s), C is the solubility of the solid in the fluid (m^3/m^3), S is the mean thickness of the grain boundary fluid phase (m), Ω is the molar volume of the solid phase (m^3/mol), R is the universal gas constant (8.31 J mol^{-1} K^{-1}), and T is the absolute temperature (K). The term $f_d(\varphi)$ is a dimensionless function of porosity that accounts for changes in grain contact area (hence contact stress magnitude) and transport path length, as porosity evolves. Following *Spiers et al*. [2004] [see also *Pluymakers and Spiers*, 2014], for porosities in the range of 5–40%, the geometry of a regular grain pack allows the approximation

$$f_d(\varphi) \approx 1/(q - 2\varphi)^2 \tag{30}$$

Similarly, the shear strain rate accommodated by pressure solution can be expressed as

$$\dot{\gamma}_{ps} = B_d \frac{DCS}{d^3} \frac{\tau \Omega}{RT} f_d(\varphi) \tag{31}$$

where B_d is the geometric constant appropriate for shear deformation [cf. *Rutter*, 1976; *Raj and Chyung*, 1981; *Shimizu*, 1995]. Note that these IPS equations can be applied to both the shear band and bulk portions of the gouge layer considered in our model.

3.7. Final Assembly of Controlling Equations

Coupling the full set of kinematic equations (11) and (14), energy/entropy equations (21), and rate-strengthening grain-boundary friction (27b) given above allows us to describe the frictional behavior of any granular fault gouge layer, either with a localized shear band (of relative thickness λ) or without a shear band ($\lambda = 0$). Here we rewrite the key results for a gouge with a localized shear band as follows:

$$V_{imp} - \dot{\tau}/K = L_t \left[\lambda \dot{\gamma}_{ps}^{sb} + (1-\lambda)\dot{\gamma}_{ps}^{bulk}\right] + L_t \lambda \dot{\gamma}_{gr} \tag{32a}$$

$$\dot{\varphi}^{sb}/\left(1-\varphi^{sb}\right) = (\tan\psi)\dot{\gamma}_{gr} - \dot{\varepsilon}_{ps}^{sb} \tag{32b}$$

$$\tau = \frac{\widetilde{\mu} + \tan\psi}{1 - \widetilde{\mu}\tan\psi}\sigma_n \tag{32c}$$

$$\widetilde{\mu} = \widetilde{\mu}^* + a_{\widetilde{\mu}} \ln\left(\dot{\gamma}_{gr}/\dot{\gamma}_{gr}^*\right) \tag{32d}$$

Note that since the granular flow (grain boundary slip) process is assumed to occur in the shear band only, the term $\dot{\gamma}_{gr}^{sb}$ in the above equations can be taken as equal to $\dot{\gamma}_{gr}$. These equations ((32a), (32b), (32c), (32d)), combined with the compaction and shear creep laws for pressure solution ((29) and (31)), describe the frictional behavior of the carbonate fault gouge as represented in Figure 2. For the special case that shear deformation is uniformly distributed, one can simply put $\lambda = 1$ in (31).

At steady state, the structure, hence porosity and dilatation angle, characterizing the granular gouge must be constant, so that $\dot{\varphi} = 0$ (32b). This means that the parallel processes of dilatation due to granular flow and compaction by pressure solution exactly balance each other, such that $\dot{\varepsilon}_{ps} = -\dot{\varepsilon}_{gr}$. For a transient jump in velocity at otherwise constant P-T conditions etc., let us say an upstep such as that imposed in a typical velocity stepping frictional test, equation (32a) implies that the shearing material will dilate ($\dot{\varphi} > 0$) instantaneously and continuously but at decreasing dilation rate. The shear stress supported will concomitantly rise abruptly according to the direct effect associated with our grain contact sliding model expressed in equation (32c) and subsequently decrease until a new steady state is reached ($\dot{\varphi} = 0$). By contrast, for an SHS test,

when sliding is stopped, the gouge will compact immediately ($\dot{\varphi} < 0$) and will be accompanied by relaxation in shear stress due to the operation of pressure solution at grain contacts. As sliding resumes, the gouge will dilate, causing an instantaneous increase in strength determined by (32a) and (32c), followed by slip weakening until a new steady state is achieved.

4. Model Implementation

4.1. Solution Method

In order to compute the frictional behavior implied by our model, the governing equations above must be solved numerically. For easy programming, we rewrite (32a)–(32d) in the form of two coupled ordinary differential equations, specifying the rates of change of shear stress (τ) and porosity (φ) (i.e., defining strength and state changes) as follows:

$$\dot{\tau}/K = V_{\text{imp}} - L_t\left[\lambda\dot{\gamma}_{\text{pl}}^{\text{sb}} + (1-\lambda)\dot{\gamma}_{\text{pl}}^{\text{bulk}}\right] - L_t\lambda\dot{\gamma}_{\text{gr}}^{*}\exp\left[\frac{\tau(1-\tilde{\mu}^{*}\tan\psi) - \sigma_n(\tilde{\mu}^{*}+\tan\psi)}{a_{\tilde{\mu}}(\sigma_n+\tau\tan\psi)}\right] \tag{33a}$$

$$\frac{\dot{\varphi}^{\text{sb}}}{(1-\varphi^{\text{sb}})} = \tan\psi\dot{\gamma}_{\text{gr}}^{*}\exp\left[\frac{\tau(1-\tilde{\mu}^{*}\tan\psi) - \sigma_n(\tilde{\mu}^{*}+\tan\psi)}{a_{\tilde{\mu}}(\sigma_n+\tau\tan\psi)}\right] - \dot{\varepsilon}_{\text{pl}}^{\text{sb}} \tag{33b}$$

We used the solvers embedded in the finite element analysis package COMSOL to do this. This package can solve both ordinary and partial differential equations. We used COMSOL because in the future we expect to need to incorporate partial differential equations describing other processes, such as pore fluid diffusion and frictional heating, into the model. Shear stress (τ) and porosity (φ) evolution were computed by numerical integrating with respect to time. In each time step employed, all variables were iterated sequentially until an accurate solution was found (within a relative tolerance of $1{:}10^6$). To simulate our lab experiments, which consisted of sequential velocity stepping and SHS testing phases (Figure 1), we entered load point velocity at fixed temperature ($T = 80°C$) and constant effective normal stress ($\sigma_n = 50$ MPa) as input to our model, obtaining shear strength and porosity as a function of time (or displacement) as output.

4.2. Input Parameters

The input parameters used in obtaining reference case solutions to our model are listed in Table 1 and described below. Based on the microstructure observed in our experiments (Figure 2) [see also *Chen et al*., 2015a], we use $\lambda = 0.0625$ and $L_t = 0.8$ mm, implying a 50 μm thick shear band. The average grain sizes in the bulk gouge and shear band are taken as 20 μm and 2 μm, respectively. The initial porosity of the bulk gouge is set to be 32%, as estimated from the mass and grain density of the experimental gouge (2.4 g with a density of 2700 kg/m^3). For the shear band, we allow the model to find a steady state porosity for a given imposed velocity and then use this porosity as the initial porosity for subsequent transient modeling. The parameter q reflects the critical state porosity φ_c for pure granular flow and plays its role via the term $(q - 2\varphi)$. Here we take q to be 0.8 for the bulk gouge, following the values used by *Niemeijer and Spiers* [2007] and *Pluymakers and Spiers* [2014] for similar grain size material. To account for the effect of the wider range in (log) grain size observed in the shear bands, which generally reduces q and hence dilatancy angle at given porosity [e.g., *Al Hattamleh et al*., 2013], we use $q = 0.4$ for the shear band. Regarding the stiffness (K) of the testing machine used in our experiments, this was calibrated at systematically varied confining pressures and temperatures. For the experimental conditions modeled here (65 MPa confining pressure and 80°C), the appropriate value of K is 5.993×10^{10} Pa/m. The grain contact friction coefficient for carbonate fault gouge is set to be 0.60 at a reference sliding velocity of 1 μm/s, consistent with the overall level of frictional strength typically exhibited by calcite gouges [*Verberne et al*., 2013b]. Using values from our experiments and the published data for calcite, we get the rate-dependent coefficient $\left(a_{\tilde{\mu}}\right)$ within a reasonable range (0.001–0.03, see supporting information for details). In our modeling, the $a_{\tilde{\mu}}$ value is set to be 0.006, consistent with the direct effects observed in the VS sequences of our experiments [*Chen et al*., 2015a].

Some parameters are poorly constrained in our model. The geometric parameter H falls in the range of $1/\sqrt{3}$ to $\sqrt{3}$ as specified earlier for a 2-D grain pack [*Niemeijer and Spiers*, 2007] but can be as low as 0.36 in a 3-D model. For our reference case calculations, we used $H = 1/\sqrt{3}$ (Table 1). The geometric constants A_d and B_d are taken to be equal, with values varying from 30.6 for uniaxial compaction to 183 for isotropic 3-D

Table 1. List of Parameters and Reference Case Values Used in the Present Model[a]

Parameter	Description (Unit)	Value (Range)	Data Source and Additional Information[b]
σ_n	effective normal stress (Pa)	5×10^{7}	experimentally applied value
T	temperature (K)	353	experimental temperature
K	machine stiffness (Pa/m)	5.993×10^{10}[c]	calibrated machine value
V_{imp}	load point velocity (m/s)	$(0.1–10)\times10^{-6}$	experimentally applied values
L_t	thickness of the gouge layer (m)	8×10^{-4}	value from experiments
λ	localization degree	0.0625 (0.0125–0.188)	value observed in experiments [*Verberne et al.*, 2013b; *Chen et al.*, 2015a]
$\varphi_0^{\mathrm{bulk}}$	initial porosity of bulk gouge	0.32	experimentally observed value
d^{sb}	average grain size of shear band (m)	2×10^{-6} (1×10^{-7}–5×10^{-6})	middle range of observed values
d^{bulk}	average grain size of the bulk gouge (m)	2×10^{-5}	mean value of the observed range
q^{sb}	2 × critical porosity for shear band	0.4	assumed here
q^{bulk}	2 × critical porosity for bulk gouge	0.7	assumed here
z	grain coordination number	6	*Spiers et al.* [2004]
H	geometrical parameter	0.577 (0.36–1.73)	assumed here following *Niemeijer and Spiers* [2007]
A_d	geometric constant for compaction by IPS	100	value for uniaxial compaction [*Pluymakers and Spiers*, 2014]
B_d	geometric constant for shear by IPS	100	as above
DS	Product of diffusion coefficient D times mean grain boundary fluid thickness S (m^3/s)	2×10^{-20} (10^{-19}–10^{-20})	*Nakashima* [1995], *Renard et al.* [1997], *Zhang et al.* [2010], and *Koelemeijer et al.* [2012]
C	solubility of the solute in fluid film (m^3/m^3)	3.95×10^{-6} [c]	*Plummer and Busenberg* [1982]
Ω	molar volume of solid phase (m^3/mol)	3.69×10^{-5}	*Plummer and Busenberg* [1982]
$\widetilde{\mu}^*$	reference grain boundary friction coefficient for velocity of 1×10^{-6} m/s	0.6	assumed here
$a_{\widetilde{\mu}}$	coefficient for logarithmic rate dependence of grain boundary friction	0.006 (0.004–0.008)	experimentally obtained [*Chen et al.*, 2015a]

[a]Other symbols used are explained in the text.
[b]All experimentally derived values were obtained from *Chen et al.* [2015a], except where stated.
[c]These parameters are temperature dependent, and here we use the values at 80°C.

compaction [*Pluymakers and Spiers*, 2014]. Lastly, compaction and shear strain rates due to diffusion-controlled IPS are determined by the magnitude of *DCS* (see equations (21) and (24a)–(24c)). From the empirical equation given by *Plummer and Busenberg* [1982], the solubility of calcite at the conditions modeled is 3.95×10^{-6} m^3/m^3. Note that unlike most other minerals, the solubility of calcite (C) decreases with increasing temperature. The product DS was estimated directly from pressure solution experiments on calcite ([*Zhang et al.*, 2010]; see also halite [*Koelemeijer et al.*, 2012]) but can also be evaluated from independent estimates of D [*Nakashima*, 1995] and S [*Renard et al.*, 1997], giving values in the range 10^{-19}–10^{-20} m^3/s (Table 1).

5. Modeling Results and Comparison With Experiments

5.1. Steady state Shearing and Parametric Sensitivity Analysis

We start with modeling steady state shearing behavior of the shear band, in which the time derivatives of shear stress $(\dot{\tau})$ and porosity $\left(\dot{\varphi}^{\mathrm{sb}}\right)$ are zero. For the velocities investigated in this study (V_{imp} = 0.1–10 μm/s), the deformation accommodated by the shear component of pressure solution is negligible. As an approximation, equations (32d) and (33a) accordingly become

$$V_{\mathrm{imp}} = L_t\lambda\dot{\varepsilon}_{\mathrm{ps}}^{\mathrm{sb}}/\tan\psi_{\mathrm{ss}} \tag{34a}$$

$$\tau_{\mathrm{ss}} = \frac{\widetilde{\mu}+\tan\psi_{\mathrm{ss}}}{1-\widetilde{\mu}\tan\psi_{\mathrm{ss}}}\sigma_n \tag{34b}$$

These imply that at steady state, the sliding velocity and the IPS-induced compaction rate in the shear band $\left(\dot{\varepsilon}_{\mathrm{ps}}^{\mathrm{sb}}\right)$ decide the state of the internal gouge material, measured in terms of ψ or φ and hence the shear resistance (τ) offered by the band. As sliding velocity increases, shear-induced dilatation occurs until again balanced at steady state by pressure solution compaction, which increases in rate as the porosity (φ) increases. This dilatation generates higher φ, lower a_c, and lower ψ at steady state, which leads to lower frictional strength as slip proceeds. At the same time, as sliding velocity increases, the grain boundary

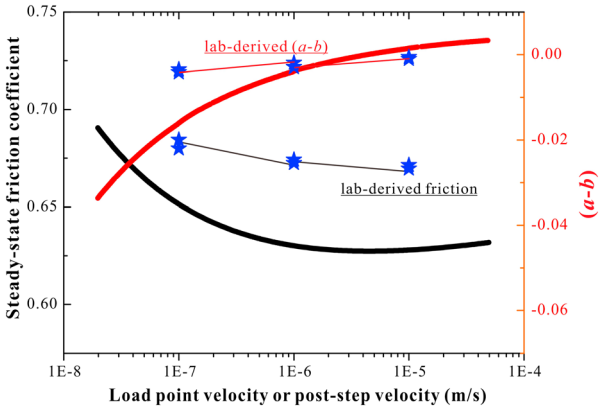

Figure 5. Modeling results for steady state friction coefficient and (*a*-*b*) as a function of load point velocity, obtained using the reference state parameter values given in Table 1. The lab-derived data reported by *Chen et al.* [2015a] for wet carbonate gouge sheared at the same T-σ_n conditions ($T = 80$°C and $\sigma_n = 50$ MPa) are added for comparison.

sliding rate and hence grain boundary friction ($\tilde{\mu}$) increase, leading to higher frictional strength. The resulting steady state frictional strength of the material is determined by the competing influence of these two effects.

Using the reference case parameter values given in Table 1, we calculated the steady state friction coefficient ($\mu_{ss} = \tau_{ss}/\sigma_n$) as a function of load point velocity (V_{imp}) from equations (34a) and (34b). As shown in Figure 5, μ_{ss} decreases with increasing velocity, indicating velocity-weakening behavior, and as velocity continues to increase, μ_{ss} starts to slightly increase, indicating weak velocity-strengthening behavior. The corresponding values of $(a-b) = \Delta\mu_{ss}/\Delta\ln(V)$ increase with increasing velocity, and lie between −0.017 and +0.001, for velocity steps imposed in the range of velocities investigated in our lab experiments (0.1–10 μm/s). All these features are consistent with the trends seen in our experimental data for carbonate gouge sheared in VS mode at 80–140°C and $\sigma_n = 50$ MPa [*Verberne et al.*, 2013b; *Chen et al.*, 2015a] and are in order-of-magnitude agreement quantitatively (refer Figure 5). Given the straightforward basis for choosing the values of the parameters used, we consider this to be acceptable agreement.

To gain insight into the properties of the model, we performed a parametric analysis to investigate the sensitivity of the computed behavior to the parameters used (i.e., to H, λ, d^{sb}, DS, $\tilde{\mu}^*$, and q^{sb} and $a_{\tilde{\mu}}$), varying these parameters in realistic ranges. As shown in Figure 6, the modeling results indicate the steady state friction strength exhibits a strong dependence on the geometric factor (H, Figure 6a), the grain size (d^{sb}, Figure 6b), the reference grain contact friction coefficient ($\tilde{\mu}^*$, Figure 6c), the extent of slip localization (λ, Figure 6d), and the grain boundary diffusivity product (DS, Figure 6e), but little dependence on the geometric constant q^{sb} (Figure 6c), which determines the reference porosity level of the shear band. In particular, variations in $\tilde{\mu}$ vertically translate the model predictions of steady state strength (Figure 6c). The model also predicts significantly lower steady state strength for larger grain size (Figure 6b) and more localized slip (Figure 6d), with these effects becoming more pronounced at lower velocities. Changing the $a_{\tilde{\mu}}$ value only slightly changes the slope of the curves (Figure 6f). As shown later, this parameter has a significant effect on the transient behavior when subjected to an abrupt change in velocity boundary conditions. By adjusting $\tilde{\mu}^*$ and other parameter(s) such as d^{sb} within small, reasonable ranges, the modeled frictional strength can be fitted quantitatively to the experimental results (Figure 7). Good agreement between modeled and measured frictional strength and (*a*-*b*) values can be obtained, for example, by choosing an intrinsic grain contact friction coefficient $\tilde{\mu}$ of 0.64–0.67 (specifically 0.655) and a shear band grain size d^{sb} of 4 μm (see Figure 7). Purely varying H or λ cannot predict the observed frictional strength. However, doing so in combination with small variations in DS and/or d^{sb} yields close agreement between the model- and lab-derived μ_{ss} and (*a*-*b*) values, within the sliding velocity investigated (0.1–10 μm/s) (Figure 7). We note, however, that manipulating these (or the many other) parameters to produce a good fit has little value other than to demonstrate that the model offers a viable (but not necessarily unique) explanation for the steady state frictional behavior observed in our experiments.

5.2. Transient Response to Velocity Stepping

For comparison with our lab experiments (VS-seq1, Figure 1), we modeled a velocity stepping sequence employing individual velocity steps of $1 \rightarrow 10 \rightarrow 1 \rightarrow 0.1 \rightarrow 1$ μm/s, taking $T = 80$°C and $\sigma_n = 50$ MPa (Figure 8a), and using the reference case parameter values employed in the steady state calculations presented in Figure 5. The results show a transient frictional strength response that is closely similar to the experimental observations for VS-seq1 (see Figures 1a and 8b) and consistent with the type of response

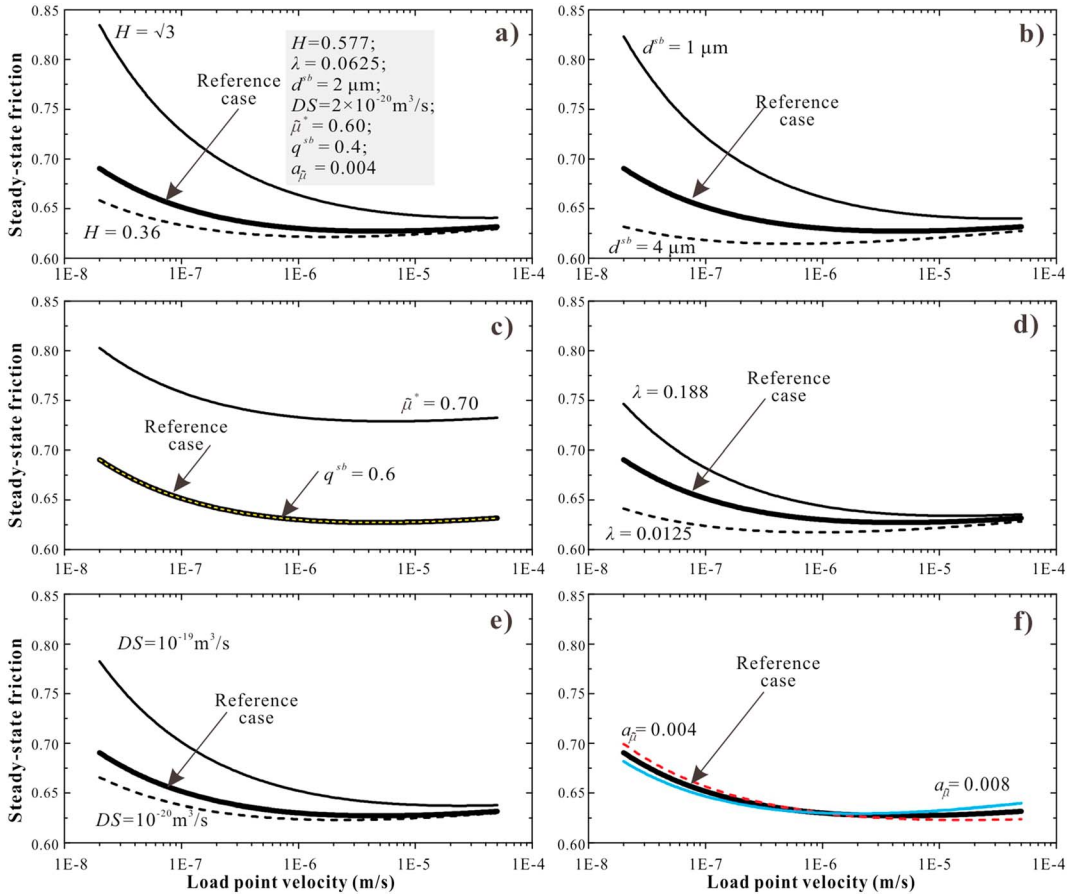

Figure 6. Sensitivity of computed steady state friction coefficient to variation in parameter values (H, λ, d^{sb}, DS, $\tilde{\mu}^*$, q^{sb}, and $a_{\tilde{\mu}}$). Note that the reference case employs the parameter values $H = 0.577$, $\lambda = 0.0625$, $d^{sb} = 2\ \mu m$, $DS = 2 \times 10^{-20}\ m^3/s$, $\tilde{\mu}^* = 0.6$, $q^{sb} = 0.4$, and $a_{\tilde{\mu}} = 0.006$. All parameter values used are listed in Table 1.

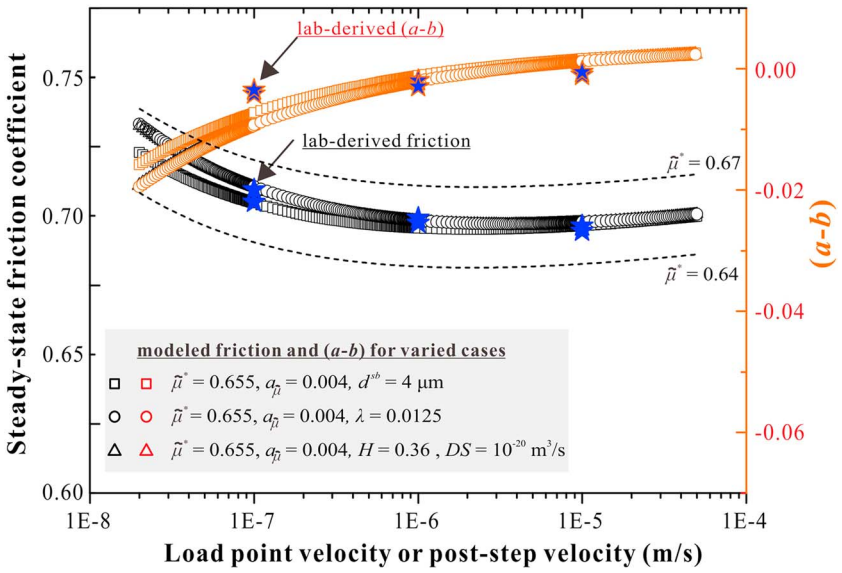

Figure 7. Good fit of the model to the lab data, for both μ_{ss} and (a-b), obtained using parameter values adjusted in reasonable ranges from the reference case, as described in the main text. The experimental data for gouge sheared at the reference T-σ_n conditions [*Chen et al.*, 2015a] are included for comparison.

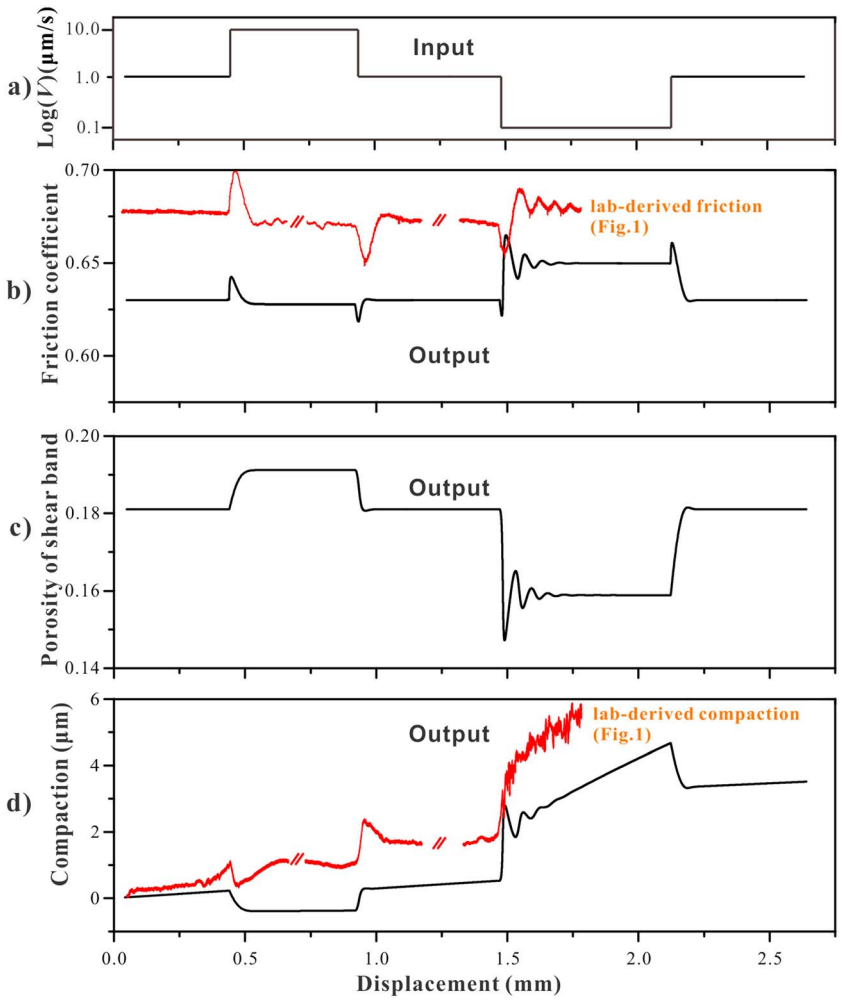

Figure 8. Modeling results for velocity stepping sequences, replicating the conditions of our VS experiments (VS-seq1) performed on wet carbonate gouge at $T = 80°C$ and $\sigma_n = 50$ MPa [see *Chen et al.*, 2015a]. (a) Velocity step sequence entered as input to the model, (b) frictional response, (c) shear band porosity, and (d) total compaction of the gouge layer. Typical experimental data are added to Figures 8b and 8d for comparison (VS-seq1, Figure 1). Note that for sake of comparison, the curves of experimental data versus displacement are laid out with breaks, since the displacements of individual V-steps imposed in our experiments are smaller than those of the modeled steps.

obtained using a classical RSF law. For each velocity step, the frictional strength exhibits first a direct effect and then evolves to a new steady state, consistent with velocity-weakening behavior (Figure 8b). The characteristic displacement associated with the modeled evolution effect is around 0.15 mm compared with ~0.18 mm in our experiments. For downsteps in sliding velocity from 1 to 0.1 μm/s, small fluctuations occur before attaining the new steady state. All of these features are seen in our lab experiments (Figures 1a and 8b). Moreover, alongside the transient changes in shear strength toward lower and higher values, our model results show that the active shear band dilates or compacts respectively, causing small increases and decreases in porosity of the shear band (Figure 8c). To compare with the macroscopic volumetric changes measured in our experiments, we calculate the total compaction of the sample, with the rate being expressed as $\dot{\varepsilon}_t = \lambda\dot{\varepsilon}_t^{sb} + (1-\lambda)\dot{\varepsilon}_t^{bulk}$. Integration of this expression gives the net cumulative compaction for the whole sample as a function of time or displacement. As shown in Figure 8d, the predicted gouge compaction exhibits stepped variations between adjacent V steps, with trends similar to that observed for the whole gouge layer in our experiments, though the magnitude is smaller. The discrepancy can be attributed either to the underestimate of shear band thickness in our reference modeling case (50 μm and can be as wide as 150 μm, Table 1) or to the dilatant response of the bulk gouge which is inhibited in the present model.

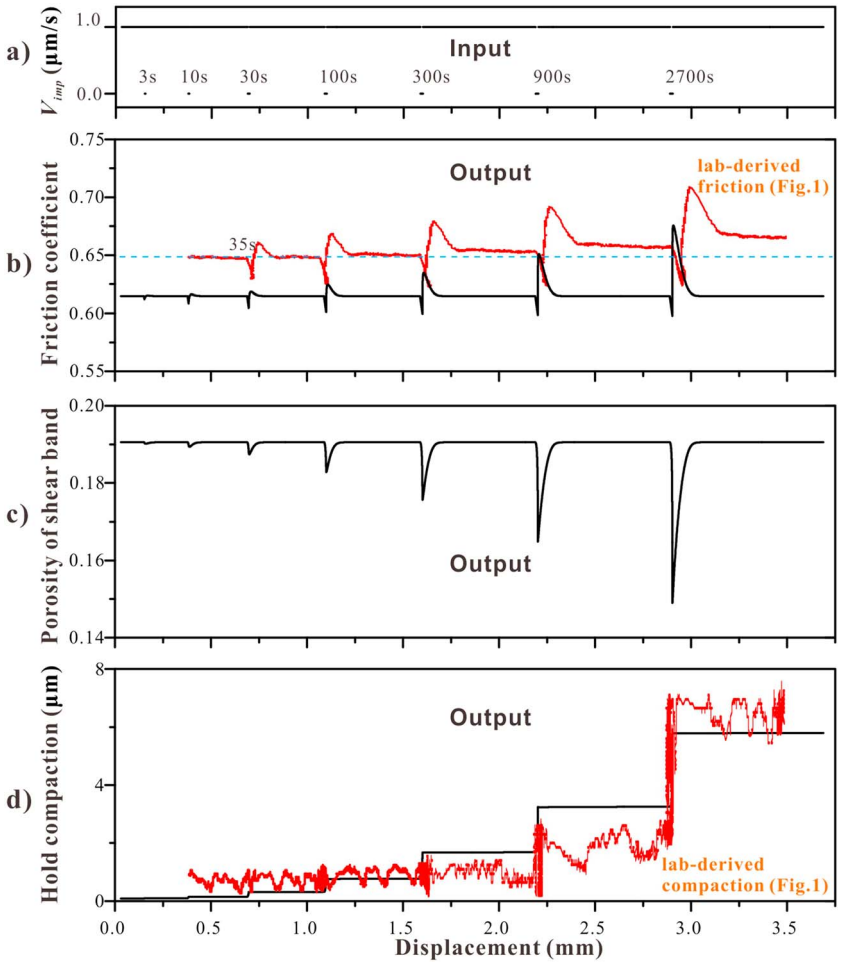

Figure 9. Modeling results for a slide-hold-slide testing sequence as executed in our experiments on carbonate gouge at $T = 80$°C and $\sigma_n = 50$ MPa [see *Chen et al.*, 2015a]. (a) Input sliding velocities and hold times. (b) Friction coefficient versus displacement. (c) Shear band porosity versus displacement. (d) Cumulative hold-time compaction of the whole sample. Experimental results from Figure 1 are added to Figures 9b and 9d for comparison.

5.3. Response to Slide-Hold-Slide Testing

Again, replicating the procedure and conditions employed in our lab experiments (Figures 1a and 1b), we modeled a SHS test sequence consisting of eight individual SHS events with hold times increasing from 3 to 2700 s in threefold jumps (Figure 9a), again using the reference case parameter values given in Table 1. Plots showing the evolution of frictional strength, shear band porosity, and total compaction predicted by our model are shown in Figures 9b–9d. The following main features of the computed friction-displacement curve are consistent with classic SHS test results [e.g., *Marone*, 1998a] and with our lab data (Figure 1b). First, our model predicts stress relaxation during hold periods, followed by an instantaneous increase in shear resistance on reloading and by a subsequent gradual decay to steady state. Second, the magnitudes of each stress relaxation event and of each subsequent transient peak healing ($\Delta\mu_{pk}$) event increase with hold time. Our model predicts that the shear band will compact during individual hold periods and dilate upon reshear, especially after long hold periods (Figure 9c). The predicted cumulative sample compaction (bulk plus shear band) during the hold time is qualitatively consistent with our lab data (Figure 9d).

Despite this broad agreement between our model and experimental results on SHS response, a clear difference is also visible, namely, in relation to the stepwise increase in steady state friction coefficient that occurs after each reshearing event in our experiments. In our modeling results, no such increase in steady state friction occurs. Rather, the steady state frictional strength before and after each SHS event remains the same (Figure 9b), while the shear band porosity returns to the original steady state level upon reshearing

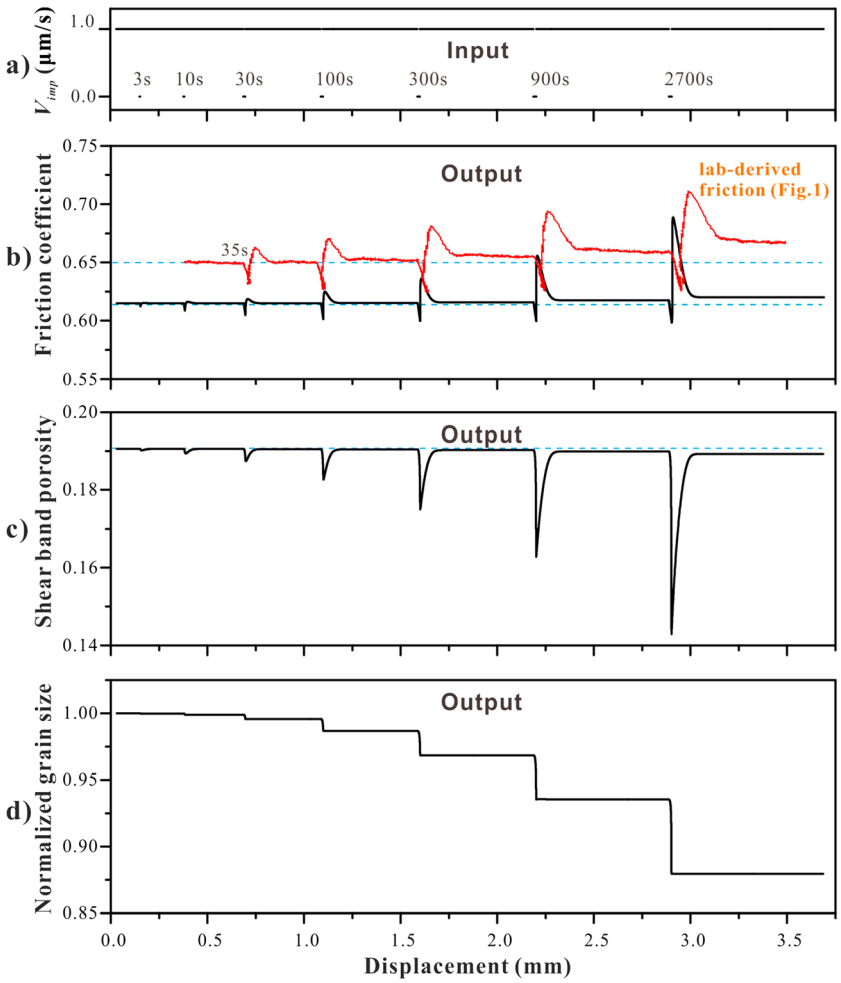

Figure 10. Modeling results for slide-hold-slide testing allowing for grain size reduction $\Delta d/d$ during each hold-reshearing event, occurring in proportion to the compactional strain ($\Delta\varepsilon$) accumulated in the shear band during the hold period (i.e., such that $\Delta d/d = c\Delta\varepsilon$ where $c \approx 1$). (a) Input sliding velocity and hold times. (b) Calculated friction coefficient versus displacement (note the gradual increase in steady state friction after reshear). (c) Calculated shear band porosity versus displacement. (d) Calculated normalized grain size ($\Delta d/d$) versus displacement. Lab-derived friction coefficients are added to Figure 10b for comparison (see Figure 1 and *Chen et al*. [2015a]).

(Figure 9c). As shown in Figure 9d, our model predicts that progressive compaction of the whole sample during hold periods causes a reduction in total porosity. However, in the present model this is not expected to affect shear strength, as that is determined by the shear band. It follows, then, from our parametric analysis (Figure 6) that the increase in steady state friction seen in our SHS sequence can likely be attributed to stepwise changes in shear band grain size (d^{sb}), shear localization degree (λ), or the sensitivity of shear band dilatation to porosity (H) occurring during relaxation or upon reshearing during SHS testing.

On the basis of microstructural examination of our experimental samples, we can immediately eliminate changes in the degree of shear localization at the sample boundary from the above list of possibilities. This is because our model shows that a broadening of 10 times would be needed to account for the observed increases in steady state friction coefficient per SHS event. No such broadening is seen in experimentally deformed samples subjected to SHS testing compared to velocity stepping only [*Chen et al*., 2015a]. We likewise eliminate purely packing-related changes in the parameter H as causing the observed increase in steady state strength, because the compaction strains (porosity reduction) occurring in the shear band, as predicted by our model for stress relaxation during hold periods, are far too small to significantly change the granular packing microstructure (Figure 9c).

Let us therefore consider the possibility of a reduction in the mean, shear band grain size (d^{sb}) in more detail. Feasible mechanisms for this include cataclasis occurring within the boundary shear band during reshearing, or perhaps mass removal from the shear band by diffusion as the shear band compacts by IPS during relaxation. Such effects could conceivably also lead to a permanent increase in H in active shear bands. To crudely incorporate grain size reduction within the shear band into our model, we make the assumption that the extent of grain size reduction ($\Delta d/d$) by either cataclasis (due to restrengthening) or mass removal (by diffusion during relaxation) will be directly related to the extent of IPS compaction occurring during relaxation. To capture such a relation in the simplest possible way, we assume that $\Delta d/d = c\Delta\varepsilon^{sb}$, where ε^{sb} is the compaction strain prediction predicted to occur in the shear band by our model in each hold period and where c is a constant of order 1. Including this in our model calculation (measuring $\Delta\varepsilon^{sb}$ with respect to shear band thickness before SHS testing) produces the results shown in Figure 10. These agree more favorably with our experimental data, supporting grain size reduction as a possible explanation of the increase in μ_{ss} seen our SHS tests (Figure 10b).

Making use of the modeling results plotted in Figure 10, i.e., incorporating the grain size reduction effect on reshearing, we now examine the predicted shear stress relaxation results for different SHS events (Figure 11a). These show that the average modeled relaxation and hence creep rate is much higher in the early, shorter hold periods than that in the later, longer holds. This reflects a systematic decrease in evolution effect with increasing hold time and relaxation strain. In our model, this is caused by the decrease in porosity that occurs due to compaction of the static shear band by IPS during each hold (refer equations (28) and (30)). Similar results have been observed in our experiments (Figure 11b) and in other studies where pressure solution was thought to be active [e.g., *Niemeijer et al*., 2008].

Finally, we derive the frictional healing parameters (Figure 1c) from our modeling predictions of Figure 10, for SHS behavior with grain size reduction upon reshearing. The results (Figure 12) indicate a nonlinear increase in transient restrengthening or peak healing ($\Delta\mu_{pk}$) with logarithm of hold time. Similar "non-Dieterich type" frictional healing behavior (i.e., not fitting equation (2)) occurred in our experiments (Figure 1) and has also been observed in SHS experiments on both quartz and halite, where it was attributed to contact area growth through pressure solution [*Nakatani and Scholz*, 2004; *Yasuhara et al*., 2005; *Niemeijer et al*., 2008]. In our model, the effect is due to shear band compaction by pressure solution during hold periods, resulting in an increase in dilation angle (refer equation (3)). Our modeling results allowing for grain size reduction upon reshearing also show a nonlinear increase in residual, persistent strengthening ($\Delta\mu_r$) with $\log(t_h)$ (Figure 12). However, in our lab experiments, the $\Delta\mu_r$ showed this increase only after the early holds and then leveled off after longer, later holds (Figure 1b) [see also *Chen et al*., 2015a]. In our modeling to date, the maximum hold time investigated is 2700 s, so that the effect of long hold times has not yet been explored.

6. Discussion and Conclusions

Building upon the microphysical modeling work of *Niemeijer and Spiers* [2007] and *den Hartog and Spiers* [2014], who addressed steady state friction, we have established a microphysical theory and numerical model describing both the transient and steady state frictional behavior of a monomineralic, velocity weakening, granular fault gouge composed of a solid phase capable of undergoing IPS. We have compared the predictions of this model with lab experiments on wet carbonate gouge as reported by *Chen et al*. [2015a]. As demonstrated by this comparison (Figures 5–12), our modeling results successfully capture all of the main features and trends by our lab experiments, by rock friction experiments in general, and by classical RSF models, including the "direct effect," "evolution effect," "stress relaxation," and "restrengthening."

In a broader sense, our theoretical analysis provides governing equations ((32a)–(32d) or (33a) and (33b)) that describe the frictional behavior of any granular fault gouge deforming by granular flow plus a grain scale creep mechanism. A key condition required for the model to be applied is that a finite amount of porosity must exist in the gouge material or can be created and modified by dilatation due to shearing. The present model predicts velocity-weakening behavior at the slip rates investigated (0.1–10 μm/s), which originates from competition between shear-induced dilatancy and compaction by pressure solution. Velocity-strengthening behavior is predicted by the model at high sliding velocity where critical state granular flow occurs, due to the rate dependence of grain boundary friction implied by our model for the atomic-scale interactions occurring within sliding grain contacts (Figure 7). Note that in the extreme case that porosity is near zero, our model will translate into a velocity-strengthening flow law for grain-scale creep,

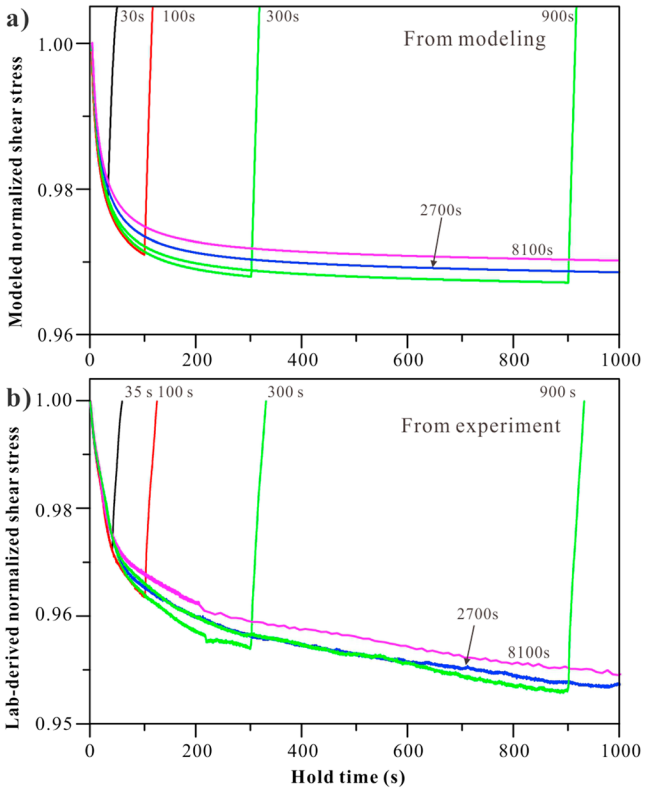

Figure 11. (a) Calculated versus (b) lab-derived curves showing the shear stress supported during stress relaxation as a function of hold time for individual holds periods, plus the abrupt increase in strength during subsequent reloading. All shear stresses are normalized with respect to the steady state stress supported immediately prior to initiating the corresponding hold.

though this has not been explicitly addressed in the present paper. Actually, at the slip rates (0.1–10 μm/s) and temperature ($T = 80°C$) investigated in our experiments and model, the shear component of IPS at grain contacts in the localized shear band is negligible relative to the imposed sliding rates $\left(\dot{\gamma}_{ps}^{sb} << \dot{\gamma}_t\right)$. According to our modeling results, at a slip rate of 0.1 μm/s, the shear component of IPS in the shear band contributes to only 2.5% the applied slip rate, while at a slip rate of 0.01 μm/s, this value increases to 5%. Our model further predicts that as the slip rate decreases to 3.2×10^{-10} m/s (10 mm/yr), the porosity of the shear band approaches zero. As such, the grain boundary sliding becomes negligible, and the deformation will be fully controlled by the pressure solution. In this case, dilatant granular flow of the bulk gouge might be activated and cause slip delocalization, depending on the strength of the bulk gouge versus the shear band. A similar transition from friction to flow with decreasing sliding rate has been previously observed in

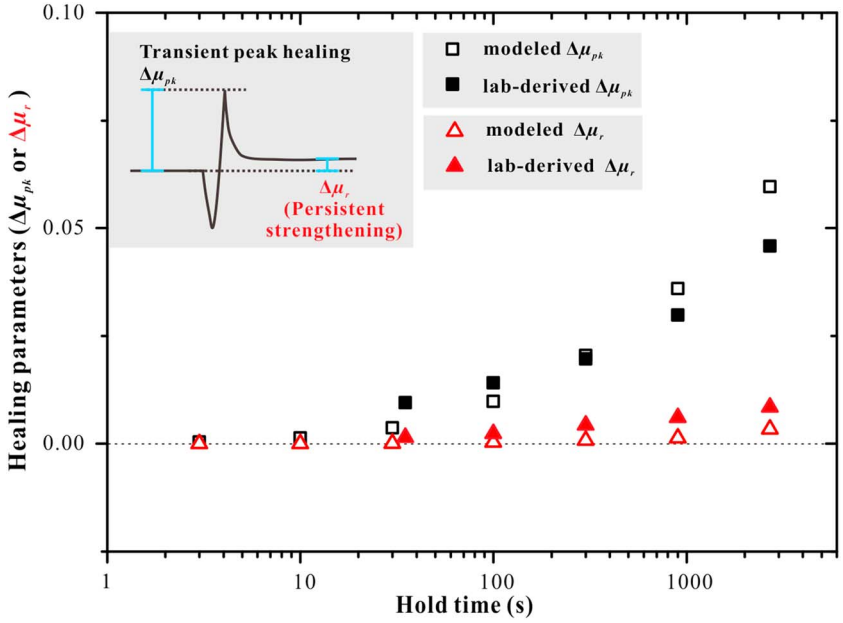

Figure 12. Frictional healing ($\Delta\mu_{pk}$ and $\Delta\mu_r$) calculated as a function of the logarithm of hold time, as derived from the modeled SHS results shown in Figure 9. Data derived from experimental result shown in Figure 1 are added for comparison [also, see *Chen et al.*, 2015a].

halite [*Shimamoto*, 1986], halite-phyllosilicate [*Bos and Spiers*, 2002] and serpentine [*Moore et al*., 1997] gouges, and the resultant change in (apparent) frictional rate dependence (i.e., from velocity weakening to velocity strengthening) has also been more recently observed and predicted by *Niemeijer and Spiers* [2006] and by *den Hartog and Spiers* [2014]. This reminds us that caution is needed when extrapolating lab-derived (a-b) values to natural seismogenic zones, where the fault slip rates are of the order of typical plate velocities of ~10^{-9} m/s or even less and are thus 3–5 orders of magnitude lower than typically imposed in lab experiments. Besides changes in velocity, it is also important to mention that if the ambient P-T conditions or specific fault rock composition favor plastic deformation (e.g., by pressure solution), velocity strengthening will be also predicted [*Verberne et al*., 2014].

Besides carbonate fault rocks, our model can be applied to a wide variety of materials sheared under a broad range of conditions with the operation of different deformation mechanisms. To address such situations, information is needed on the most appropriate deformation mechanism and corresponding creep law to describe grain-scale creep, especially if pressure solution is not dominant. More robust information and preferably direct experimental measurements on grain contact frictional strength $(\tilde{\mu})$ are also needed to underpin our grain boundary friction model or to provide an alternative. We can then apply the overall model to predict the steady state frictional strength and transient evolution thereof for any fault material in response to any imposed boundary conditions. Recognizing that other grain-scale deformation mechanisms can be incorporated in the model as an alternative creep process, we believe that our model embodies the key physics underlying the RSF-type behavior and the RSF law.

To our knowledge, our theory is the first to be able to model full RSF-type behavior in terms of realistic, microstructurally verifiable processes and state variables (such as porosity), without using the RSF law (note that *Sleep et al*. [2000] incorporated the strain delocalization/localization hence porosity changes into a classical RSF law, in a phenomenological sense, in order to describe the evolution of the state variable but with no mechanistic basis). It can accordingly provide a significantly improved basis for extrapolation of lab-derived friction data to natural conditions. However, many further improvements still need to be made. These include (1) analytical derivation of the RSF parameters a, b, (a-b), D_c, and β; (2) a linear stability analysis to obtain slip instability parameters such as critical stiffness K_c and the critical recurrence wavelength W_c for unstable growth from small perturbations to steady sliding [cf., *Scholz*, 2002]; (3) incorporation of other creep mechanisms for grain-scale creep besides pressure solution and incorporation of time-/rate-dependent grain contact cementation or cohesion effects; (4) application of the model to variable normal stress conditions; (5) including the effect of dilatation associated with activation of granular flow, for example, during the formation of new shear bands [cf. *Marone*, 1990]; (6) incorporation of the effects of increasingly important shear creep behavior at low or zero porosity, resulting in velocity strengthening at high-temperature and/or low load point velocity. Moreover, the present model only applies to grain-supported granular materials and needs further modification to be applicable to matrix-supported materials. Some of these advances have already been initiated in steady state models [*den Hartog and Spiers*, 2014], but they need extending to the transient case. In a future paper, we will derive analytical expressions for a, b, (a-b), D_c, and β in terms of evolving state variables from the present model, and we will apply our model to extrapolate our lab data on carbonate gouge to examine the implications for the seismic cycle on active faults in limestone terrains, including the middle-northern portion of the Longmenshan fault.

Acknowledgments
Jianye Chen was funded by the China NSF (41372202), the Basic Scientific Funding of Chinese National Nonprofit Institutes (IGCEA1405), and also by European Research Council starting grant SEISMIC (335915). We thank John Platt, an anonymous reviewer, and the Associate Editor for their review and positive feedback on this paper. We note that there are no data sharing issues since all of the numerical results shown in the figures are produced by solving the equations, and all the input data are cited and referred to in the reference list. The input files necessary to reproduce the results are available from the authors upon request (jychen@ies.ac.cn).

References

Al Hattamleh, O. H., H. H. Al-Deeky, and M. N. Akhtar (2013), The consequence of particle crushing in engineering properties of granular materials, *Int. J. Geosci.*, *4*, 1055–1060.

Ampuero, J.-P., and A. M. Rubin (2008), Earthquake nucleation on rate-and-state faults: Aging and slip laws, *J. Geophys. Res.*, *113*, B01302, doi:10.1029/2007JB005082.

Barbot, S., Y. Fialko, and Y. Bock (2009), Postseismic deformation due to the M_w 6.0 2004 Parkfield earthquake: Stress driven creep on a fault with spatially variable rate-and-state friction parameters, *J. Geophys. Res.*, *114*, B07405, doi:10.1029/2008JB005748.

Baumberger, T., P. Berthoud, and C. Caroli (1999), Physical analysis of state- and rate-dependent friction law, II. Dynamic friction, *Phys. Rev. B.*, *60*(6), 3928–3939.

Beeler, N. M., T. E. Tullis, and J. D. Weeks (1994), The roles of time and displacement in the evolution effect in rock friction, *Geophys. Res. Lett.*, *21*, 1987–1990, doi:10.1029/94GL01599.

Beeler, N. M., T. E. Tullis, and J. D. Weeks (1996), Frictional behavior of large displacement experimental faults, *J. Geophys. Res.*, *101*, 8697–8715, doi:10.1029/96JB00411.

Berthoud, P., T. Baumberger, C. G'Sell, and J.-M. Hiver (1999), Physical analysis of the state- and rate-dependent friction law: Static friction, *Phys. Rev. B.*, *59*(22), 14,313–14,327.

Bos, B., and C. J. Spiers (2002), Fluid-assisted healing processes in gouge bearing faults: Insights from experiments on a rock analogue system, *Pure Appl. Geophys.*, *159*, 2537–2566, doi:10.1007/s00024-002-8747-2.
Carpenter, B. M., M. M. Scuderi, C. Collettini, and C. Marone (2014), Frictional heterogeneities on carbonate-bearing normal faults: Insights from the Monte Maggio Fault, Italy, *J. Geophys. Res. Solid Earth*, *119*, 9062–9076, doi:10.1002/2014JB011337.
Chen, J., B. A. Verberne, and C. J. Spiers (2015a), Interseismic re-strengthening and stabilization of carbonate faults by "non-Dieterich" healing under hydrothermal conditions, *Earth Planet. Sci. Lett.*, *423*, 1–12.
Chen, J., B. A. Verberne, and C. J. Spiers (2015b), Effects of healing on the seismogenic potential of carbonate fault rocks: Experiments on samples from the Longmenshan Fault, Sichuan, China, *J. Geophys. Res. Solid Earth*, *120*, 5479–5506, doi:10.1002/2015JB012051.
Chen, T., and N. Lapusta (2009), Scaling of small repeating earthquakes explained by interaction of seismic and aseismic slip in a rate and state fault model, *J. Geophys. Res.*, *114*, B01311, doi:10.1029/2008JB005749.
Chester, F. M. (1994), Effects of temperature on friction: Constitutive equations and experiments with quartz gouge, *J. Geophys. Res.*, *99*, 7247–7261, doi:10.1029/93JB03110.
Campbell, C. S. (2006), Granular material flows—An overview, *Powder Technol.*, *162*, 208–229, doi:10.1016/j.powtec.2005.12.008.
den Hartog, S. A. M., and C. J. Spiers (2013), Influence of subduction zone conditions and gouge composition on frictional slip stability of megathrust faults, *Tectonophysics*, *600*, 75–90.
den Hartog, S. A. M., and C. J. Spiers (2014), A microphysical model for fault gouge friction applied to subduction megathrusts, *J. Geophys. Res. Solid Earth*, *119*, 1510–1529, doi:10.1002/2013JB010580.
De Meer, S., and C. J. Spiers (1997), Uniaxial compaction creep of wet gypsum aggregates, *J. Geophys. Res.*, *102*, 875–891.
Dieterich, J. H. (1972), Time-dependent friction in rocks, *J. Geophys. Res.*, *77*, 3690–3697, doi:10.1029/JB077i020p03690.
Dieterich, J. H. (1979), Modeling of rock friction: 1. Experimental results and constitutive equations, *J. Geophys. Res.*, *84*, 2161–2168, doi:10.1029/JB084iB05p02161.
Hetland, E. A., M. Simons, and E. M. Dunham (2010), Post-seismic and interseismic fault creep I: Model description, *Geophys. J. Int.*, *181*, 81–98.
Ikari, M. J., D. M. Saffer, and C. Marone (2009), Frictional and hydrologic properties of clay-rich fault gouge, *J. Geophys. Res.*, *114*, B05409, doi:10.1029/2008JB006089.
Ikari, M. J., B. M. Carpenter, and C. Marone (2016), A microphysical interpretation of rate- and state-dependent friction for fault gouge, *Geochem. Geophys. Geosyst.*, *17*, 1660–1677, doi:10.1002/2016GC006286.
Karner, S. L., C. Marone, and B. Evans (1997), Laboratory study of fault healing and lithification in simulated fault gouge under hydrothermal conditions, *Tectonophysics*, *277*, 41–55.
Koelemeijer, P. J., C. J. Peach, and C. J. Spiers (2012), Surface diffusivity of cleaved NaCl crystals as a function of humidity: Impedance spectroscopy measurements and implications for crack healing in rock salt, *J. Geophys. Res.*, *117*, B01205, doi:10.1029/2011JB008627.
Lehner, F. K. (1990), Thermal dynamics of rock deformation by pressure solution, in *Deformation Processes in Minerals, Ceramics and Rocks*, edited by D. J. Barber and P. G. Meredith, pp. 296–333, Unwin Hyman, London.
Lehner, F. K., and J. Bataille (1984), Nonequilibrium thermodynamics of pressure solution, *Pure Appl. Geophys.*, *122*, 53–85.
Liteanu, E., A. Niemeijer, C. J. Spiers, C. J. Peach, and J. H. P. de Bresser (2012), The effect of CO_2 on creep of wet calcite aggregates, *J. Geophys. Res.*, *117*, B03211, doi:10.1029/2011JB008789.
Logan, J. M., C. A. Dengo, N. G. Higgs, and Z. Z. Wang (1992), Fabrics of experimental fault zones: their development and relationship to mechanical behavior, in *Fault Mechanics and Transport Properties of Rocks*, edited by B. Evans and T. F. Wong, pp. 33–67, Academic Press, London.
Marone, C. (1990), Frictional behavior and constitutive modeling of simulated fault gouge, *J. Geophys. Res.*, *95*, 7007–7025, doi:10.1029/JB095iB05p07007.
Marone, C. (1998a), The effect of loading rate on static friction and the rate of fault healing during the earthquake cycle, *Nature*, *391*, 69–72.
Marone, C. (1998b), Laboratory-derived friction laws and their application to seismic faulting, *Annu. Rev. Earth Planet. Sci.*, *26*, 643–696, doi:10.1146/annurev.earth.26.1.643.
Marone, C., J. E. Vidale, and W. Ellsworth (1995), Fault healing inferred from time dependent variations in source properties of repeating earthquakes, *Geophys. Res. Lett.*, *22*, 3095–98, doi:10.1029/95GL03076.
Mitsui, N., and P. Ván (2014), Thermodynamic aspects of rock friction, *Acta Geod. Geophys.*, *49*, 135–146.
Moore, D. E., D. A. Lockner, S. Ma, R. Summers, and J. D. Byerlee (1997), Strengths of serpentinite gouges at elevated temperatures, *J. Geophys. Res.*, *102*, 14,787–14,801, doi:10.1029/97JB00995.
Muhuri, S. K., T. A. Dewers, T. E. Scott Jr., and Z. Reches (2003), Interseismic fault strengthening and earthquake-slip instability: Friction or cohesion? *Geology*, *31*, 881–884, doi:10.1130/G19601.1.
Nakashima, S. (1995), Diffusivity of ions in pore water as a quantitative basis for rock deformation rate estimates, *Tectonophysics*, *245*, 185–203.
Nakatani, M. (2001), Conceptual and physical clarification of rate and state friction: Frictional sliding as a thermally activated rheology, *J. Geophys. Res.*, *106*, 13,347–13,380, doi:10.1029/2000JB900453.
Nakatani, M., and C. H. Scholz (2004), Frictional healing of quartz gouge under hydrothermal conditions: 1. Experimental evidence for solution transfer healing mechanism, *J. Geophys. Res.*, *109*, B07201, doi:10.1029/2001JB001522.
Niemeijer, A. R., and C. J. Spiers (2006), Velocity dependence of strength and healing behaviour in simulated phyllosilicate-bearing fault gouge, *Tectonophysics*, *427*, 231–253.
Niemeijer, A. R., and C. J. Spiers (2007), A microphysical model for strong velocity weakening in phyllosilicate-bearing fault gouges, *J. Geophys. Res.*, *112*, B10405, doi:10.1029/2007JB005008.
Niemeijer, A. R., C. J. Spiers, and B. Bos (2002), Compaction creep of quartz sand at 400–600°C: experimental evidence for dissolution-controlled pressure solution, *Earth Planet. Sci. Lett.*, *195*, 261–275.
Niemeijer, A. R., C. Marone, and D. Elsworth (2008), Healing of simulated fault gouges aided by pressure solution: Results from rock analogue experiments, *J. Geophys. Res.*, *113*, B04204, doi:10.1029/2007JB005376.
Niemeijer, A. R., C. Boulton, V. G. Toy, J. Townend, and R. Sutherland (2016), Large-displacement, hydrothermal frictional properties of DFDP-1 fault rocks, Alpine Fault, New Zealand: Implications for deep rupture propagation, *J. Geophys. Res. Solid Earth*, *121*, 624–647, doi:10.1002/2015JB012593.
Noda, H. (2008), Frictional constitutive law at intermediate slip rates accounting for flash heating and thermally activated slip process, *J. Geophys. Res.*, *113*, B09302, doi:10.1029/2007JB005406.
Noda, H. (2016), Implementation into earthquake sequence simulations of a rate- and state-dependent friction law incorporating pressure solution creep, *Geophys. J. Int.*, *205*, 1108–1125.
Paterson, M. S. (1995), A theory for granular flow accommodated by material transfer via an intergranular fluid, *Tectonophysics*, *245*, 135–151.

Plummer, L. N., and E. Busenberg (1982), The solubilities of calcite, aragonite and vaterite in CO_2-H_2O solutions between 0 and 900°C, and an evaluation of the aqueous model for the system $CaCO_3$-CO_2-H_2O, *Geochim. Cosmochim. Acta*, *46*, 1011–1040.

Pluymakers, A. M. H., and C. J. Spiers (2014), Compaction creep of simulated anhydrite fault gouge by pressure solution: theory v. experiments and implications for fault sealing, in *Rock Deformation from Field, Experiments and Theory: A Volume in Honour of Ernie Rutter*, *Special Publications*, vol. 409, edited by D. R. Faulkner, E. Mariani, and J. Mecklenburgh, Geological Society, London, doi:10.1144/SP409.6.

Raj, R., and C. K. Chyung (1981), Solution-precipitation creep in glass ceramics, *Acta Metall.*, *29*, 19–166.

Renard, F., P. Ortoleva, and J. P. Gratier (1997), Pressure solution in sandstones: Influence of clays and dependence on temperature and stress, *Tectonophysics*, *280*, 257–266.

Renard, F., A. Park, P. Ortoleva, and J. P. Gratier (1999), A transitional pressure solution model, *Tectonophysics*, *312*, 97–115.

Rice, J. R., and A. L. Ruina (1983), Stability of steady frictional slipping, *J. Appl. Mech.*, *105*, 345–349.

Rice, J. R., N. Lapusta, and K. Ranjith (2001), Rate and state dependent friction and the stability of sliding between elastically deformable solids, *J. Mech. Phys. Solids*, *49*(9), 1865–1898.

Rubin, A. M., and J. P. Ampuero (2005), Earthquake nucleation on (aging) rate-and-state faults, *J. Geophys. Res.*, *110*, B11312, doi:10.1029/2005JB003686.

Ruina, A. (1983), Slip instability and state variable laws, *J. Geophys. Res.*, *88*, 10,359–10,370, doi:10.1029/JB088iB12p10359.

Rutter, E. H. (1976), The kinetics of rock deformation by pressure solution, *Philos. Trans. R. Soc. London*, *A283*, 203–219.

Rutter, E. H. (1983), Pressure solution in nature, theory and experiment, *J. Geol. Soc. London*, *140*, 725–740.

Scholz, C. H. (2002), *The Mechanics of Earthquakes and Faulting*, 471 pp., Cambridge Univ. Press, Cambridge, U. K.

Shimamoto, T. (1986), Transition between frictional slip and ductile flow for halite shear zones at room temperature, *Science*, *231*, 711–714.

Shimizu, I. (1995), Kinetics of pressure solution creep in quartz: Theoretical considerations, *Tectonophysics*, *245*, 121–134.

Sleep, N. H., E. Richardson, and C. Marone (2000), Physics of strain localization in synthetic fault gouge, *J. Geophys. Res.*, *105*, 25,875–25,890, doi:10.1029/2000JB900288.

Spiers, C. J., S. De Meer, A. R. Niemeijer, and X. Zhang (2004), Kinetics of rock deformation by pressure solution and the role of thin aqueous films, in *Physicochemistry of Water in Geological and Biological Systems*, edited by S. Nakashima et al., pp. 129–158, Univ. Acad. Press, Inc., Tokyo.

Tse, S. T., and J. R. Rice (1986), Crustal earthquake instability in relation to the depth variation of frictional slip properties, *J. Geophys. Res.*, *91*, 9452–9472, doi:10.1029/JB091iB09p09452.

Tullis, T. E., and J. D. Weeks (1987), Micromechanics of frictional resistance of calcite, *Eos Trans. AGU*, *68*, 405.

Verberne, B. A., J. H. P. De Bresser, A. R. Niemeijer, C. J. Spiers, D. A. Matthijs de Winter, and O. Plümper (2013a), Nanocrystalline slip zones in calcite fault gouge show intense crystallographic preferred orientation: Crystal plasticity at subseismic slip rates at 18–150°C, *Geology*, *41*, 863–866.

Verberne, B. A., C. J. Spiers, A. R. Niemeijer, J. H. P. De Bresser, D. A. M. De Winter, and O. Plümper (2013b), Frictional properties and microstructure of calcite-rich fault gouges sheared at sub-seismic sliding velocities, *Pure Appl. Geophy.*, *171*, 2617–2640.

Verberne, B. A., O. Plümper, D. A. M. De Winter, and C. J. Spiers (2014), Superplastic nanofibrous slip zones control seismogenic fault friction, *Science*, *346*, 1342–1344.

Yasuhara, H., C. Marone, and D. Elsworth (2005), Fault zone restrengthening and frictional healing: The role of pressure solution, *J. Geophys. Res.*, *110*, B06310, doi:10.1029/2004JB003327.

Zhang, X., C. J. Spiers, and C. J. Peach (2010), Compaction creep of wet granular calcite by pressure solution at 28°C to 150°C, *J. Geophys. Res.*, *115*, B09217, doi:10.1029/2008JB005853.